In-situ monitoring of sintering and analytical modeling of densification and shrinkage in binder jetted 316L stainless steel

Mohammad Jamalkhani [a], Zhifang Deng [b], Dominick Sossong [a], Iman Dashtgerd [a], Greg Martiska [c], Amir Mostafaei [a,*]

[a] Department of Mechanical, Materials, and Aerospace Engineering, Illinois Institute of Technology, 10 W 32nd Street, Chicago, IL 60616, USA

[b] Erik Jonsson School of Engineering and Computer Science, The University of Texas at Dallas, 800 W Campbell Rd, Richardson, TX 75080, USA

[c] Mercury Scientific Inc., 64 Barnabas Road #1, Newtown, CT 06470, USA

[*] Corresponding author: A. Mostafaei (mostafaei@iit.edu)

Abstract

In binder jetting, shrinkage and deformation occur during the sintering step, both of which are affected by the green density of the binder jetted materials. The study innovatively introduces a cost-effective, practical, and in-process monitoring system for visualizing shrinkage and deformation on larger samples than conventionally observed using small-scale specimens in dillatometry equipment. The powder characteristics and binder jet printing process itself influence the initial green density. The comprehensive analysis of powder flowability and packing density, densification behavior, and shrinkage reveals that the consolidated parts using virgin powder (with a green density of 55%) can achieve a relative density above 99.9% with an anisotropic shrinkage in the Z>X>Y direction. In contrast, the used or recycled powder exhibits a lower green density of ~48%, higher shrinkage rate in all three dimensions, and a decreased degree of anisotropy. Using in-process imaging and experimental data on the grain size attained through optical microscopy and electron backscatered diffraction imaging, the material's shear and bulk viscosities were determined. The formation of delta-ferrite and its impact on densification were discussed in the context of solid-state and supersolidus liquid phase sintering. The model relied on the continuum sintering theory formulated by Skorohod and Olevsky. The strain evolution from the in-situ imaging of sintering process is correlated with porosity based on the used feedstock and applied sintering temperatures. The outcomes of this study offer valuable perspectives on anisotropic sintering mechanisms, bridging the knowledge gap regarding the relationships between structures produced through binder jetting and subsequent sintering of materials.

Keywords: Additive manufacturing; Powder characteristics; Shrinkage; Microstructure analysis; Mathematical modeling.

1. Introduction

In powder bed additive manufacturing (AM) processes, it is crucial to monitor powder characteristics, including morphology, particle size distribution (PSD), rheology, and contaminants (such as C, O, N), especially when powders are recycled [1–7]. During binder jetting, powder encounters binder agglomerates, altering the particle size distribution (PSD). This, in turn, affects powder flowability and packing density. Typically, spherical powder with a narrow PSD enhances both powder flowability and powder bed packing density [8,9]. Monitoring powder chemistry, particularly changes in C, O, and N contents, is crucial to minimize deviations in sintering behavior, phase formation at elevated temperature, and

densification. However, contradictory opinions have been reported for different metal alloys, such as alloy 718, Ti-6Al-4V [10], and 17-4 PH steel [11], used in powder bed fusion AM processes. Mirzababaei et al. [3] studied recycled 316L stainless steel (SS) powders used in binder jetting. Recycled powder generally exhibits improved flowability due to a reduction in fine particles. Additionally, there is a slight enhancement in powder flowability linked to the increased presence of coarser powders. Furthermore, there is typically a slight increase in C and O concentrations observed in recycled powder. However, the powder packing density tends to decrease due to the lower presence of fine powders [12–14].

As a multi-step AM technique, binder jetting operates by depositing layer upon layer of powder feedstock and selectively binding them using a liquid polymer. After printing, curing step is needed to enhance strength in binder jetted components thus parts can be handled and placed in a furnace for consolidation [15–17]. During the printing step, interactions between the binder and powder result in the formation of interlayer voids and printing lines. This occurs due to the ballistic ejection of powder from the surface and the displacement of powder beneath the surface, leaving sub-surface voids and a continuous gap between the deposited layers [18,19]. Sintering is a typical densification process in the binder jetting of metallic components. Given that the relative green part density is ~50-60%, binder jetted components undergo volumetric shrinkage ranging from 50% to 40% [16].

Sintering is a critical step in the sinter-based AM processes, impacting the quality of components through significant densification. Over decades, researchers have conducted analytical and experimental studies to understand sintering behavior, including pore evolution, shrinkage, and grain size. Frenkel's initial theory [20] on particle coalescence due to surface tension formed the basis for subsequent analytical models, including various material responses such as viscoplastic [21] and viscoelastic [22] behaviors. Constitutive models including Skorokhod's continuum mechanism [23] and Li and Häggblad's viscoplastic model [21] revealed insights into densification rates, strain, and shape changes. An integrated microscale model by Raether et al. [24] captured microstructure evolution during solid-state sintering. Olevsky and Molinari [25] developed a model to connect the sintering stress and viscosity tensors to the shrinkage of porous bodies. However, the isotropic sintering variables that govern these models, such as the strain rate tensor, stress tensor, viscous modulus, and sintering stress [26], lack the precision to accurately quantify anisotropic shrinkage in sinter-based AM components. These variables depend on factors such as powder shape, specific surface energy, relative density or pore fraction in the preform component, particle arrangement during densification, self-diffusion coefficient related to particle chemistry, and surface contamination. This complexity poses a significant challenge in understanding anisotropic sintering behavior in sinter-based AM parts. Thus, unlike traditional isotropic models, the nature of the additively manufactured components demands consideration of anisotropic shrinkage.

As a powerful tool, analytical modeling has been employed to predict anisotropic shrinkage in sinter-based 3D printed parts [27]. While some recent work, such as that by Rios et al. [28], has established isotropic parameters for pressure-less sintering in binder jetted stainless steel alloys, the assumption of isotropic shrinkage contradicts existing literature [29–34]. Experimental and numerical studies, such as those by You et al. [34] and Wang et al. [33], on the densification of extruded 3D printed stainless steel powder have demonstrated higher shrinkage of 3% in the Z-direction. Earlier research by Jamalkhani et al. [35] and Mostafaei et al. [30,36] also provided experimental insights into the reasons behind this

observed trend. It is noteworthy that the formation of sub-surface voids contributes to increased shrinkage in the Z-direction [29,31]. Additionally, studies [35,37] demonstrated that binder droplets displace powder in the bed, causing the formation of print lines on each discrete layer. Consequently, a slightly lower relative density in the X-direction compared to the Y-direction is observed. Similar observations of anisotropy in shrinkage were reported in other sinter-based AM processes such as extrusion 3D printing, fused deposition modeling, and fused fillemant fabrication [38–41]. Therefore, anisotropy and non-uniform shrinkage in sintered binder jetted components are likely, and these factors should be considered in modeling approaches.

The 316L SS alloy is categorized as an austenitic stainless steel; nevertheless, there is a possibility of a small quantity of delta-ferrite (δ-ferrite) forming at the grain boundaries. In sintered-based manufacturing processes such as powder metallurgy, extrusion 3D printing, and binder jetting, the occurrence of δ-ferrite has been observed at sintering temperatures surpassing the solidus temperature. Specifically, the introduction of a polymer binder to 316L SS powder poses the risk of carbon contamination, potentially influencing the solidus temperature and elevating the fraction of δ-ferrite at the grain boundaries [42]. The formation of the δ-ferrite phase enhances material diffusivity through two primary mechanisms. The newly formed phase possesses a body-centered cubic (BCC) structure with a higher diffusion coefficient compared to the face-centered cubic (FCC) austenitic phase. Additionally, the creation of δ-ferrite grains results in the development of new grain boundaries, thereby promoting the sintering process [43]. Consequently, the formation of this phase contributes to an elevated densification rate at high temperatures during sintering.

Previous studies suggest that δ-ferrite can enhance the strength, ductility, toughness, and resistance to thermal cracking in stainless steel [35,44,45]. It is important to note, however, that an excess of δ-ferrite (>5%) may elevate the likelihood of pitting corrosion [46,47]. Wang et al. [33] also showed the δ-ferrite could be eliminated through solution treatment at 1100 °C for 1 h. Slow cooling rate during densification of 3D printed 316L SS is also a practical way to control δ-ferrite formation at the grain boundaries [33,35]. Conversely, δ-ferrite in 316L SS has the potential to improve dislocation mobility, increase work hardening, and enhance overall ductility [35,48]. Controlling the δ-ferrite content in 316L SS is crucial due to its positive effects, especially as the alloy is increasingly used in industries like marine, nuclear, and chemical engineering.

This study aims to investigate and quantify the influence of powder characteristics on the relative green density of binder jetted 316L SS parts, followed by an analysis of densification, revealing anisotropic shrinkage. An innovative in-process imaging setup is employed to unveil the anisotropic dimensional evolution throughout the sintering stage. Microstructure analysis is then carried out to assess pore fraction, grain evolution, and phase formation. Using an analytical model established for anisotropic sintering, the correlation between pore distribution and anisotropic viscous behavior was elucidated by introducing relevant parameters associated with anisotropic viscosity. The findings of this research offer valuable insights into the sintering behavior of binder jetted parts, contributing to an enhanced comprehension of the sintering process applicable to various material systems.

2. Materials and Methods

2.1. Material – Gas-atomized 316L SS (Sandvik Osprey Co. with chemical composition of Ni=10.9 wt%, Cr=18.28 wt%, Mo=2.12, Mn=2.19 wt%, Si=0.58 wt%, C=0.03%, Fe=bal.) utilized as the feedstock under two distinct conditions: virgin and used powders. The used powder, subjected to multiple drying cycles over a span of more than a year, went through preparation in an oven and then sieving through 106 μm mesh to ensure optimal conditions for the subsequent printing cycle. The used powder has been recycled over time by blending used powder with virgin one at a ratio of 2:1 (used to virgin) every 10 cycles. The chemical analysis indicated that the used powder exhibited minimal deviation in terms of carbon (C), oxygen (O), and nitrogen (N) uptake compared to the virgin powder. This can be attributed to the storage of powder in a moisture-free environment and the adapted drying cycle applied to the powder before each printing session. The C, O, and N concentrations in the powders were quantified using LECO instruments (models TCH600 and CS744). The virgin powder was employed directly from the packaging, with a single pre-heat cycle in an oven at 185±2 °C for 8 h to enhance its readiness for use as feedstock. The PSD of these powders was analyzed based on the sampling from ~600 particles using a scanning electron microscope (SEM) model 5900LV from JEOL USA Inc. Subsequently, the particle sizes were determined through the application of ImageJ software. Regarding powder rheology, the ability of powder to flow was evaluated by measuring the power, time, and variances in energy of powder in a rotating drum (Revolution Powder Analyzer, Mercury Scientific Inc.). A camera was used to capture images of the powder at 20 frames per second within the rotation process occurred at 0.3 rpm, and then, its software analyzed the behavior of powder in flow including the potential energy, angle, surface fractal, and volume.

2.2. Processing – Cubic samples with the dimensions of 15×20×10 mm^3 were binder jetted (Innovent+ binder jet 3D printer, ExOne). The AquaFuse (BA-005 solution), a water-based binder, was deposited onto the powder bed with a 30 pL print head nozzle size, a powder bed layer thickness of 50 μm, and a saturation level of 80%. The binder application followed a schedule, settling for 8 s and then went through a 10 s drying phase for each layer. The roughing and smoothing rollers were configured to have a rotational speed of 300 rpm and 600 rpm, respectively, coupled with a traverse speed of 3 mm/s. Such process parameters were consistently maintained for printing samples using both virgin and used powder, ensuring consistency and reliability across various material conditions.

2.3. Post-process sintering – The densification process performed using a tube furnace (FT1700, 1700 °C 1-zone 60 mm tube furnace, Across International) operating under a vacuum level of approximately 10^{-5} bar. The sintering profile involved a binder burnout step at 600 °C for 1 h. Subsequently, the temperature was ramped up to the maximum sintering temperatures which inludes 1220 °C, 1340 °C, 1370 °C, and 1400 °C with an 8-h hold time. The entire sintering cycle adhered to a controlled heating/cooling rate of 5 °C/min.

2.4. In-situ imaging and data processing– This step was performed to evaluate the temperature-dependent densification behavior and viscosity of the binder jetted parts using virgin and used powder. For such an objective, the cap from one end of the tube was adjusted, allowing observation of the interior through a quartz window. Then, a DSLR Canon EOS T7 camera equipped with a Canon EF 180mm f/3.5L Macro USM Lens was employed to capture images at 1-min intervals. The camera settings were optimized for the imaging requirements, operating in aperture priority mode with an aperture set at 9.0, ISO set at 100, exposure compensation of minus 1 stop, and a White Balance configured for Tungsten lighting conditions. For each sintering temperature, two samples were sintered—one sample was

positioned to reveal the XZ plane, while the other was oriented to expose the XY plane as illustrated in Figure 1.

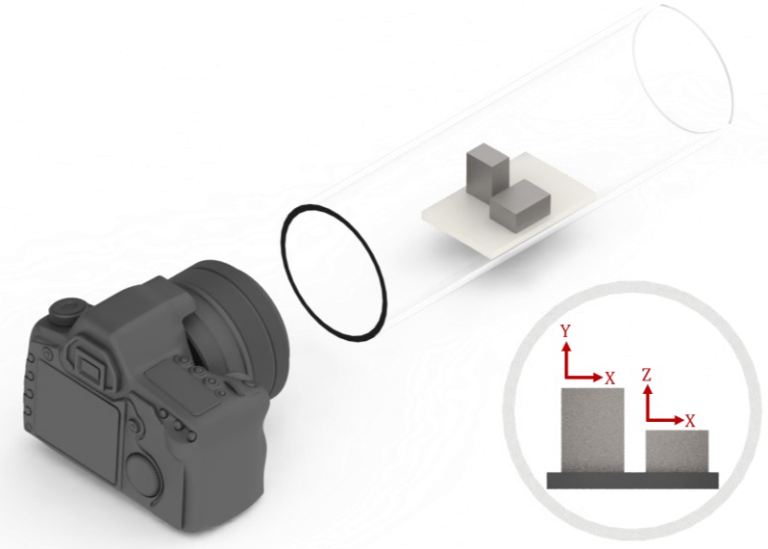

Figure 1. Schematics of post-processing test setup and the orientation of samples during the sintering process.

After capturing in-situ images, DaVinci Resolve 18, a video editing tool, was utilized to convert images into videos at a frame rate of 24. Then, a Python code implemented the Channel and Spatial Reliability Tracking (CSRT) object tracking algorithm, integrating color data with spatial reliability for precise object tracking across frames. Channel reliability manages variations in appearance from changing illumination, while spatial reliability addresses occlusions and non-rigid deformations by considering spatial and temporal coherence in the object motion. CSRT excels in tracking solid bodies during in-situ imaging of sintering experiments, addressing challenges including scale variation, color changes, and slow-motion scenarios.

The CSRT algorithm employs a Discriminative Correlation Filter to estimate object location and appearance, learning iteratively from positive and negative training samples. Sample generation involves positive samples representing the target object and negative samples capturing background or distractor objects [49]. Video tracking revolves around measuring the length of the solid body in each frame. This was achieved by selecting a Region of Interest (ROI) around each object, initializing CSRT trackers, and continuously updating their positions in each frame. The code computes strain by comparing object lengths in each frame relative to a reference length (see Equation 1-3), calculated for the X, Y, and Z axes, indicating shrinkage in the binder jetted parts in three dimensions.

$$\varepsilon_x = \frac{(l_x - l_{x0})}{l_{x0}} \quad \text{Equation 1}$$

$$\varepsilon_y = \frac{(l_y - l_{y0})}{l_{y0}} \quad \text{Equation 2}$$

$$\varepsilon_z = \frac{(l_z - l_{z0})}{l_{z0}} \quad \text{Equation 3}$$

The interactive aspect of the code involved the user selecting the baseline and ROIs in the video. This interaction defines the reference points for length measurements. Also, the

tracking process is designed to be interruptible. Enhanced graphical visualization is achieved through complementary programs.

2.5. Characterization – The surface topology of the green parts was examined using an optical microscope (Keyence VHX-7100 digital microscope). Surface roughness measurements were obtained from the top surface of both virgin and used powder samples using optical profilometry. The datasets comprised microscale profiles detailing distances and corresponding height deviations, with measurements captured at three separate horizontal lines along the sample's surface. Prior to analysis, the height data was adjusted to a zero-centered datum to account for the average height across the surface profile. This step ensured that subsequent roughness calculations were reflective of deviations from a normalized mean plane. Arithmetical mean roughness (R_a) and root-mean-square deviation (R_q) parameters were computed in accordance with ISO 4288 standards using the following equations [50]:

$$R_a = \frac{1}{l}\int_0^l |Z(x)|\,dx \approx \frac{1}{n}\sum_{i=1}^{n}|Z_i| \qquad \text{Equation 4}$$

$$R_q = \sqrt{\frac{1}{l}\int_0^l Z^2(x)\,dx} \approx \sqrt{\frac{1}{n}\sum_{i=1}^{n}{Z_i}^2} \qquad \text{Equation 5}$$

where *l* is the reference length, *n* is the number of discrete profile deviations, and $Z(x)$ takes the average height of the roughness profile.

To acquire density data, the mass and dimensions of both the green parts and sintered parts were measured. For the determination of the relative density value in the brown condition (pre-sintered in the binder debinding stage at a temperature of 600 °C with a dwell time of 1 h followed by a furnace cool down) and subsequent calculation of the pore level, two samples (one with virging powder and one with used powder) were used. The pore values obtained at this stage were considered as the initial porosity for analytical modeling. After sintering, for microstructure evaluation, samples were sliced parallel to the XZ plane, revealing observable stacking layer patterns from the printing process. Sliced samples were hot mounted using MetLab phenolic thermosetting molding powder and ground with SiC sandpapers ranging from grades 400 to P4000. Polishing was then followed through a series of steps: 3-µm diamond abrasive, 1- and 0.05-µm Al_2O_3 abrasive, and 0.04-µm colloidal silica on a platen (Buehler Phoenix 4000 Grinder Polisher). The same optical microscope (Keyence VHX-7100) was then employed to capture optical micrographs representing pore features. In addition, the microstructure was investigated using an electron backscatter diffraction (EBSD) detector, attached to the SEM (5900LV, JEOL USA Inc.). The phase analysis was conducted using MTEX, a MATLAB-based toolbox.

2.6. Analytical modeling – With the help of continuum theory of sintering [51], analytical modeling was implemented for the binder jetted 316L SS part, under different conditions including the use of different powder types (virgin and used feedstock) and sintering at various temperatures. The approach involved using a constitutive model that correlates the stress and strain rate tensors (σ_{ij} and $\dot{\varepsilon_{ij}}$) in the viscous sintering process of a porous element, as developed by Olevsky [51]:

$$\sigma_{ij} = 2\eta\left(\varphi\dot{\varepsilon}'_{ij} + \left(\psi - \frac{1}{3}\varphi\right)\dot{e}I\right) + P_L I \qquad \text{Equation 6}$$

here, η shows the viscosity for the fully dense part. The actual resistance-to-flow behavior of the porous material will be different; however, it started with understanding the fundamental properties of the non-porous material. The symbol $\dot{e}$ denotes the volume strain rate, or trace of the strain rate tensor, while φ and ψ represent the effective shear and bulk moduli for the viscosity, respectively. Both φ and ψ are pore-dependent parameters. In addition, P_L shows the sintering stress, Laplace pressure. Shrinkage is anticipated to occur solely due to this stress, given that pressure-less (vacuum) sintering conditions were applied [32]. I is a Kronecker delta function.

Under ideal conditions, the external stress becomes zero due to sintering occurring in a vacuum environment, simplifying the strain rate tensor to the following form [32]:

$$\dot{\varepsilon}'_{ij} = \begin{pmatrix} \dot{\varepsilon}_x & 0 & 0 \\ 0 & \dot{\varepsilon}_y & 0 \\ 0 & 0 & \dot{\varepsilon}_z \end{pmatrix} \quad \text{Equation 7}$$

Since analytical modeling is applied to a simple cubic component, the influence of gravity is negligible. However, if a structure with overhang features is under consideration, the impact of gravity should be taken into account in the calculations of $\dot{\varepsilon}_z$ [32].

As σ_{ij} considered to be 0, Equation *6* can be expressed in the following form:

$$2\eta\left(\varphi\dot{\varepsilon}'_{ij} + \left(\psi - \frac{1}{3}\varphi\right)\dot{e}I\right) + P_L I = 0 \quad \text{Equation 8}$$

The correlation between the pore and volumetric strain rate is stablished by employing mass conservation law to evaluate the evolution of pore as a function of the sintering time:

$$\dot{e} = \dot{\varepsilon}_x + \dot{\varepsilon}_y + \dot{\varepsilon}_z = \frac{\dot{\theta}}{1-\theta} \quad \text{Equation 9}$$

where θ is porosity and $\dot{\theta}$ is the rate at which the porosity changes.

To calculate the initial θ as the input in Equation 9, the relative density of the brown part is measured using the following equation:

$$\rho = (1-\theta) = \frac{m}{\left(L_x \cdot L_y \cdot L_z\right) \cdot \rho_{full}} \quad \text{Equation 10}$$

where m is the mass of brown part, l is the length of brown part in different directions, and ρ_{bulk} is the bulk density. For 316L SS, ρ_{bulk} was considered to be 7.99 g/cm^3 [52].

The relative density was determined to be ~55% (virgin powder) and ~48% (used powder). Therefore, the initial pore levels were calculated to be ~0.45 (virgin powder) and ~0.52 (used powder).

Two elements of φ and ψ were evaluated using the following equations [51]:

$$\varphi = (1-\theta)^2 \quad \text{Equation 11}$$

$$\psi = \frac{2}{3}\frac{(1-\theta)^3}{\theta} \quad \text{Equation 12}$$

At the macroscopic level, ψ represents the impact that the morphology of the pores within the material have on its ability to densify and reduce in volume [28]. The expression of sintering stress was generated by the capillary force acting between neighboring particles during the sintering process [28]. Subsequently, a model must be used to calculate the average of the localized stress across a larger scale of porosity, referred to as the effective stress or sintering stress. In the model proposed by Skorohod [53], the effective stress is obtained by taking the surface free energy for each unit of mass, denoted as F_s, and dividing it by the volume of the pores, V:

$$P_L = \frac{dF_s}{dV}$$ Equation 13

Next, the specific surface area, denoted by ξ, is calculated through a relationship dependent on the porosity and the average curvature of the surface, which is expressed as:

$$\xi = \frac{3}{r}\theta$$ Equation 14

Here, r stands for the radius of the powder particles (assumed that the particles are spherical). Additionally, the sintering pressure can be described in terms of the specific surface area:

$$P_L = \gamma_s \frac{\mathrm{d}\xi}{d\theta}(1-\theta)^2$$ Equation 15

Equation 15 is equivalent to:

$$P_L = \frac{6\gamma_s(1-\theta)^2}{D}$$ Equation 16

where D represents the grain size. To determine the evolution of grain size, sintering was conducted at similar maximum temperatures but with varying dwell times, including 0 min, 15 min, 30 min, 1 h, 2 h, 4 h, and 8 h. Subsequently, Boltzmann nonlinear curve fitting was employed to acquire data on the evolution of grain size during the sintering process. γ_s (mN/m) is the surface tension acting on the sintering stress and serves as a temperature-dependent parameter in Equation *19* presented in the form below [54]:

$$\gamma_s = -0.14T + 1450$$ Equation 17

where T is the temperature in Kelvin.

Since anisotropic shrinkage dominates the densification of the binder jetted parts, obtaining three-dimensional viscosity data is crucial. To achieve this, literature [32] proposed reformulating Equation 8 in a matrix format as follows:

$$-P_L\begin{pmatrix}1&0&0\\0&1&0\\0&0&1\end{pmatrix} = 2\eta\left[\varphi\begin{pmatrix}\dot{\varepsilon_x}&0&0\\0&\dot{\varepsilon_y}&0\\0&0&\dot{\varepsilon_z}\end{pmatrix} + \left(\psi - \tfrac{1}{3}\varphi\right)\begin{pmatrix}\dot{e}&0&0\\0&\dot{e}&0\\0&0&\dot{e}\end{pmatrix}\right]$$ Equation 18

Therefore, the viscosity can be derived in three dimensions of X, Y, and Z in the following form:

$$\eta_x = \frac{-P_L}{2\left[\varphi\dot{\varepsilon}_x + \left(\psi - \frac{1}{3}\varphi\right)\dot{e}\right]}$$ Equation 19

$$\eta_y = \frac{-P_L}{2\left[\varphi\dot{\varepsilon}_y + \left(\psi - \frac{1}{3}\varphi\right)\dot{e}\right]}$$ Equation 20

$$\eta_z = \frac{-P_L}{2\left[\varphi\dot{\varepsilon}_z + \left(\psi - \frac{1}{3}\varphi\right)\dot{e}\right]}$$ Equation 21

The representation of viscosity involves a general Arrhenius function that expresses its dependence on temperature [55].

$$\eta = \eta_0 \exp\left(\frac{Q}{RT}\right)$$ Equation 22

where η_0 shows the pre-exponent for viscous flow, Q denotes the activation energy, R is the universal gas constant, and T is the absolute temperature in Kelvin. By incorporating the

values of φ, ψ, and P_L from Equations 11, 12, and 16 into Equations 19-21 the resultant equations are as follows:

$$\eta_x = \frac{-3\gamma_s(1-\theta)^2}{D\left[(1-\theta)^2\dot{\varepsilon}_x + \left[\frac{2}{3}\frac{(1-\theta)^3}{\theta} - \frac{1}{3}(1-\theta)^2\right]\left(\dot{\varepsilon}_x + \dot{\varepsilon}_y + \dot{\varepsilon}_z\right)\right]} \quad \text{Equation 23}$$

$$\eta_y = \frac{-3\gamma_s(1-\theta)^2}{D\left[(1-\theta)^2\dot{\varepsilon}_y + \left[\frac{2}{3}\frac{(1-\theta)^3}{\theta} - \frac{1}{3}(1-\theta)^2\right]\left(\dot{\varepsilon}_x + \dot{\varepsilon}_y + \dot{\varepsilon}_z\right)\right]} \quad \text{Equation 24}$$

$$\eta_z = \frac{-3\gamma_s(1-\theta)^2}{D\left[(1-\theta)^2\dot{\varepsilon}_z + \left[\frac{2}{3}\frac{(1-\theta)^3}{\theta} - \frac{1}{3}(1-\theta)^2\right]\left(\dot{\varepsilon}_x + \dot{\varepsilon}_y + \dot{\varepsilon}_z\right)\right]} \quad \text{Equation 25}$$

In the field of continuum mechanics, the rheological or flow properties of materials are characterized using shear (G) and bulk (K) viscosities. These parameters are essential in establishing a proportional relationship between stress and strain rate, presented in a specific mathematical form:

$$\sigma'_{ij} = 2\mathrm{G} \cdot \dot{\varepsilon}'_{ij} \quad \text{Equation 26}$$

$$\sigma_m = \mathrm{K} \cdot \dot{\varepsilon}'_{ii} \quad \text{Equation 27}$$

Here, σ'_{ij} denotes the deviatoric (or differential) component of stress, $\dot{\varepsilon}'_{ij}$ shows the deviatoric component of strain rate, σ_m is the measure of hydrostatic (or mean) stress, and $\dot{\varepsilon}'_{ii}$ represents the rate of volumetric strain. Both G and K are temperature-sensitive constants intrinsic to the wrought material. Nevertheless, during sintering, the presence of pore modifies these viscosity values. To incorporate the influence of porosity, adjustment factors are necessary. Therefore, effective shear and bulk moduli are employed, which are functions exclusively of the porosity level [32]:

$$\mathrm{G} = \eta(\mathrm{T}) \cdot \varphi(\theta) \quad \text{Equation 28}$$

$$\mathrm{K} = 2\eta(\mathrm{T}) \cdot \psi(\theta) \quad \text{Equation 29}$$

where η denotes the temperature-dependent viscosity of the fully-densed material. There are numerous models formulated to establish the shear and bulk moduli, among which Skorohod's model is noted for its high accuracy [56]. This model treats the material as a dual-phase porous matrix, with one phase being an incompressible elastic matrix and the other phase consisting of pores. Skorohod drew parallels between the hydrodynamics in composites and the behavior of this two-phase system to initially define a correlation between shear viscosity and porosity for cases where porosity is very small (θ is much less than 1). Subsequently, Skorohod extended this relationship to account for higher porosity levels using a differential method, leading to the final formula presented in Equation 11.

Conversely, Mackenzie and Shuttleworth [53] applied a different approach by considering a spherical pore within an incompressible elastic material. From this model, they derived a formula for bulk viscosity, represented by Equation 30, which shows that bulk viscosity (K), adjusted for the presence of porosity (θ) [32]:

$$\mathrm{K} = \frac{4}{3}\mathrm{G} \cdot \frac{1-\theta}{\theta} \quad \text{Equation 30}$$

By replacing G with its expressions from Equation 28 and Equation *11*, the function ψ, which accounts for the effect of porosity on bulk viscosity, can be determined and is presented in Equation 12.

3. Results and discussions

3.1. Powder characteristics

In the context of binder jetting process, the rheological properties of the feedstock powders play a key role in determining the green density of the binder jetted product. Figure 2(A) shows morphology of the virgin and used powders. Results indicated that the population of fine particles (<5μm) deacreased in the used powder compared to the virgin one. The probability density function (PDF) graphs, plotted via Kernel Density Estimation (KDE) [3], and cumulative distribution function (CDF) graphs are illustrated in Figure 2(B). For the virgin powder, the D_{10}, D_{50}, and D_{90} values were 3.3, 7.5, and 18.0 μm, respectively; while the used powder exhibited slightly larger values of 5.2, 9.4, and 19.6 μm, respectively. This PSD analysis data confirmed a higher proportion of larger particles in the used powder, as initially suggested by the micrograph observations.

In terms of distribution spread, the standard deviation for the used powder was ~5.6 μm, suggesting a narrower range of powder sizes. In contrast, the virgin powder exhibited a slightly broader spread with a standard deviation of ~6.8 μm. Both distributions showed right-skewed characteristics, as evidenced by skewness values of ~1.2. This skewness implies a higher frequency of smaller powder sizes and a tail extending towards larger sizes. Regarding the peakedness of the distributions, used powder demonstrated a slightly higher kurtosis of 0.96 compared to 0.90 for the virgin powder, indicating distributions with relatively heavier tails but not significantly different in peakedness.

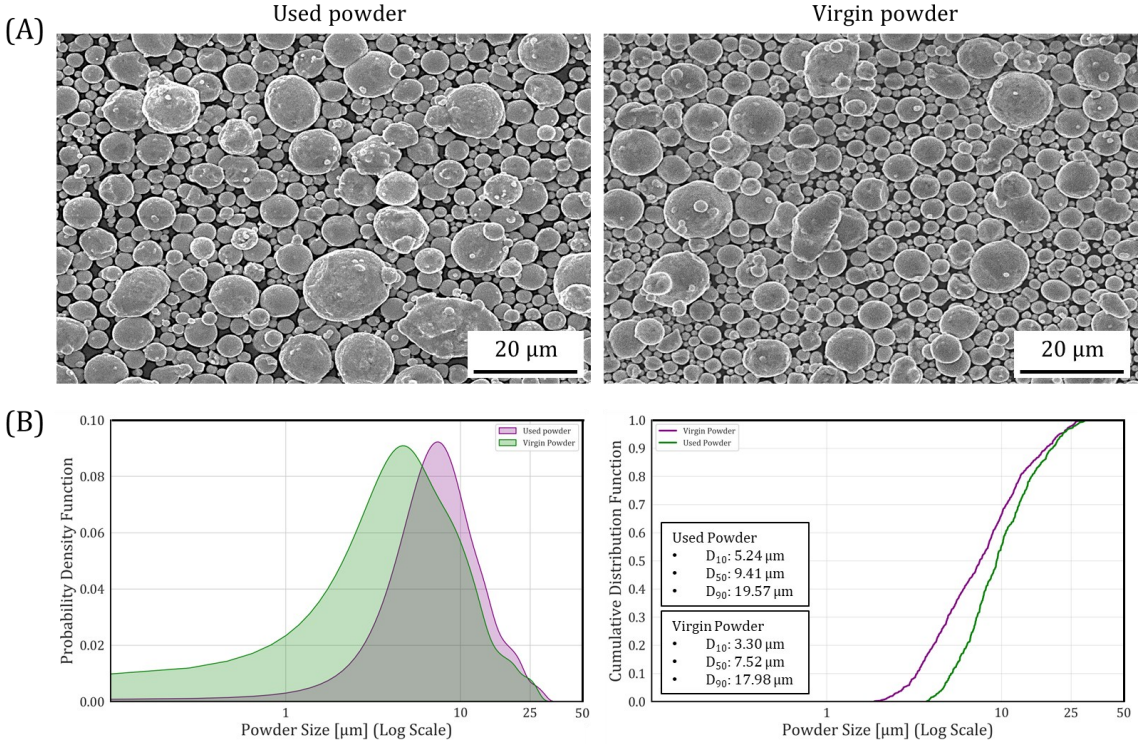

Figure 2. (A) SEM micrographs showing powder morphology and (B) particle size distribution of the used and virgin 316L SS powders.

The flowability results are summarized in Table 1, revealing notable differences in rheological characteristics of used and virgin powders. The virgin powder exhibited a significantly higher avalanche energy (33.4±18.7 mJ/kg) compared to the used powder

(19.9±10.9 mJ/kg), suggesting a more reactive nature (associated with the released avalanche angle) under comparable conditions [9]. Also, the virgin powder demonstrated a steeper avalanche angle (47.4±2.1°) and longer avalanche time (3.3±1.6 s), implying differences in flow characteristics, possibly due to higher particle cohesion of virgin powder compared to the used ones. The break energy was higher in the virgin powder (83.5±6.2 mJ/kg), indicating a greater resistance to flow initiation [6]. Furthermore, the virgin powder showed almost double the thickness (6.93 mm) and significantly higher cohesion (244.0 Pa), factors that are likely to influence its packing density and flow behavior. In terms of yield strength, the virgin powder again surpassed the used powder, recording 180.3 Pa compared to 129.8 Pa, suggesting a higher structural integrity under stress. Finally, C, O, and N content of the virgin and used powders were summarized in Table 1, suggesting a slight deviation in powder surface in which concentration of all three elements increased. The effect of initial C, O, and N content on sintering and densification of 316L SS was discussed in earlier studies in [7,35,57].

Table 1. Powder rheology characteristics and chemistry (C, O, N) of the used and virgin 316L SS powders utilized as the feedstock of the binder jetting process.

Powder rheology characteristics	Powder type	
	Used powder	Virgin powder
Avalanche energy (mJ/kg)	19.9±10.9	33.4±18.7
Avalanche angle (degrees)	43.4±3.0	47.4±2.1
Avalanche time (s)	2.2±1.3	3.3±1.6
Break energy (mJ/kg)	69.9±7.0	83.5±6.2
Thiskcness cohesion (Pa)	117.9	244.0
Yield strength (Pa)	129.8	180.3
Thickness (mm)	3.82	6.93
Dynamic density (g/cm^3)	3.69	3.68
Surface fractal	4.99	6.95
Carbon [wt.%]	0.0291	0.0250
Oxygen [wt.%]	0.1407	0.1290
Nitrogen [wt.%]	0.1210	0.1130

For avalanche energy (Figure 3(A)), the virgin powder showed a higher 50th percentile value (33.0 mJ/kg) than the used powder (20.3 mJ/kg), indicating greater energy accumulation before avalanche events. In terms of break energy (Figure 3(C)), the virgin powder consistently exhibited higher values across all percentiles (10th %=74.6 mJ/kg, 50th %=84.6 mJ/kg, 90th %=93.5 mJ/kg) compared to the used powder (10th %=62.9 mJ/kg, 50th %=69.6 mJ/kg, 90th %=84.4 mJ/kg), suggesting increased resistance to flow initiation. The surface fractal dimension analysis (Figure 3(D)) indicated that the virgin powder possessed a more complex and irregular surface (50th %=6.8) in contrast to the used powder (50th %=4.9), impacting its flow dynamics and packing behavior. Finally, the avalanche angle (Figure 3(B)) was steeper in the virgin powder (50th %=47.9°) compared to the used powder (50th %=43.5°), possibly indicating enhanced particle cohesion and distinct flow characteristics. The avalanche spectrum in Figure 3(F), representing the relationship between time and total avalanche energy, is illustrated for both powder types. The used powder showed shorter durations leading up to its peak avalanche energy, which occurred at ~1.99 s. This is indicative of a quicker transition to peak energy release during the avalanching process. The peak energy was quite high at 5787 mJ/kg, suggesting a rapid energy release over a short time frame, which may influence the compactibility and

uniformity of the powder when spread during printing. In contrast, the virgin powder exhibited a longer duration before reaching its peak energy, suggesting a more gradual energy buildup. The peak occurred at ~2.99 s, with a slightly lower maximum energy of 5698 mJ/kg. The extended duration before reaching this peak suggests that the virgin powder may have more consistent flow behavior, potentially contributing to a more uniform and controlled layering process in binder jetting. The comparison between the two powders showed that the used powder, with its shorter avalanche duration and higher peak energy, may be subjected to a more abrupt packing process [58]. This could lead to challenges in achieving uniform layer density. The virgin powder, with its longer duration and controlled peak, may enable more reliable layer formation, which is beneficial for the structural integrity and dimensional accuracy of the printed parts.

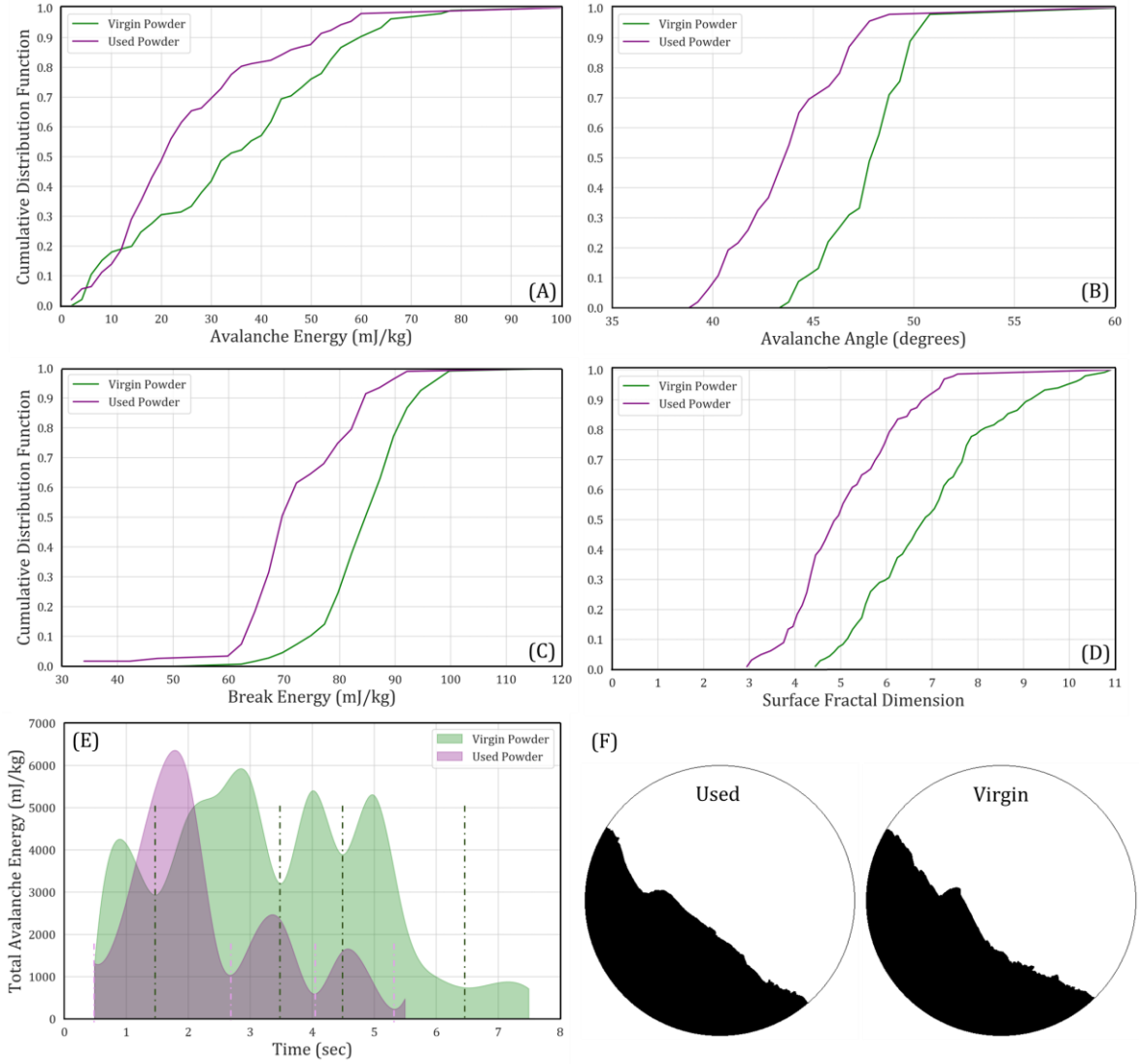

Figure 3. Cumulative distribution function (CDF) of (A) avalanche energy, (B) avalanche angle, (C) break energy, (D) surface fractal dimension, (E) avalanche spectrum (time vs total avalanche energy), and (F) exemplary snapshot illustrating powder behavior in rotating drum. Reported values in Table 1 was the analysis performed by the software.

3.2. Surface topology of binder jetted parts

Figure 4 illustrates the surface topography and roughness measurements of the green parts. Visual examination of the green part (see Figure 4(A)) using virgin powder revealed a series of uniform valleys, spaced at an interval of ~200 μm, resulting from the impact of binder jet droplets on the powder bed [35]. These orderly formations became more evident under higher magnification, as seen in the heat map micrographs (Figure 4(B)). Conversely, the green part manufactured with used powder displayed a less distinct topographical pattern when observed at low magnification, with scattered large-sized particles causing surface irregularity. High-magnification heat map micrographs in Figure 4(B) supported this finding, showing dispersed circular hot spots and barely visible print lines.

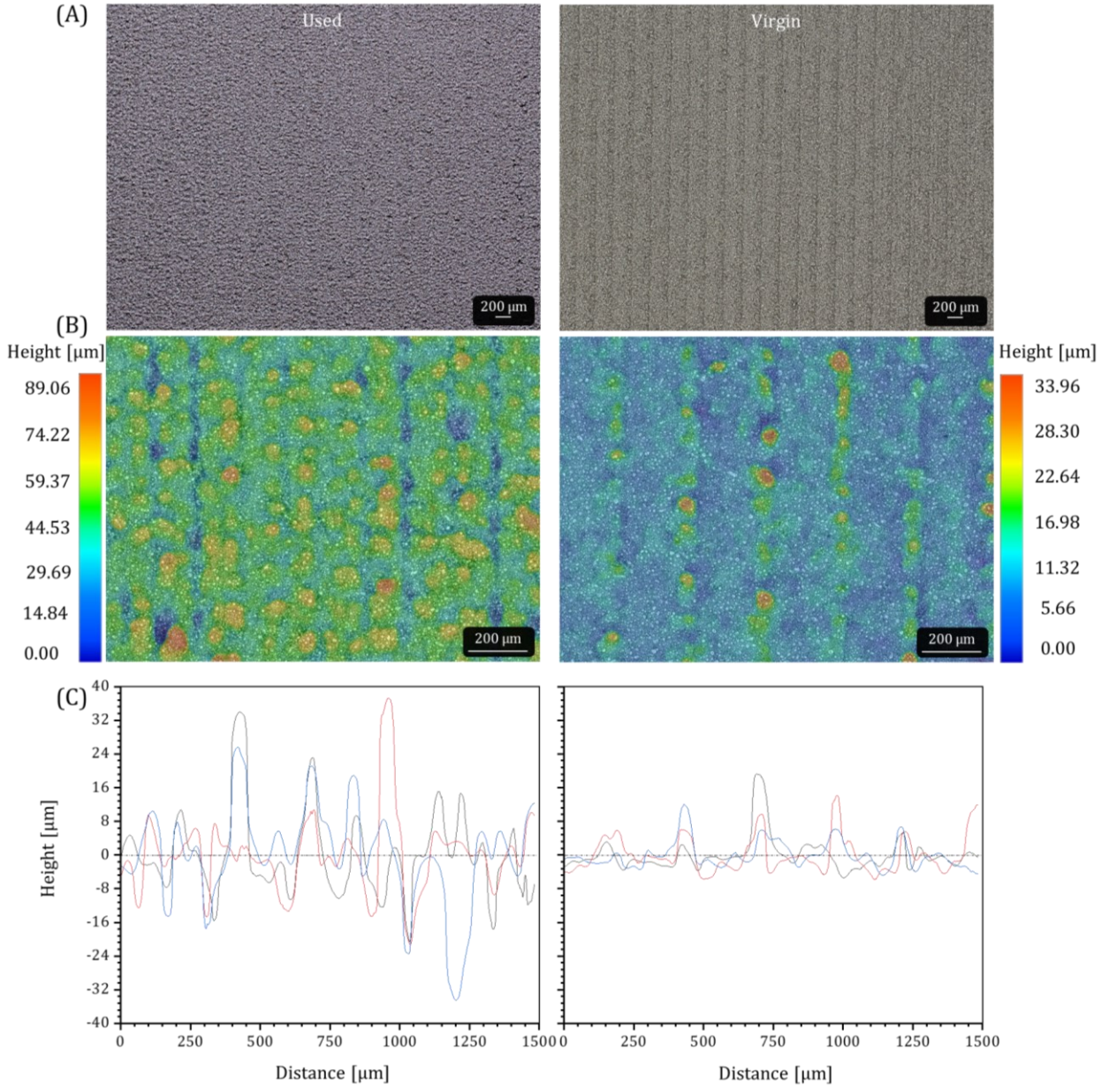

Figure 4. (A) Optical micrographs, (B) surface topography, and (C) optical profilometry plots showing roughness profile of the binder jetted green parts manufactured using virgin and used powders.

The calculations resulted in a mean R_a value of ~2.6 μm and an R_q value of ~3.8 μm for the virgin powder, indicating a relatively smooth surface characteristic. Conversely, the used powder exhibited markedly higher roughness values, with a mean R_a of ~7.1 μm and an R_q of 10.3 μm, reflective of a surface with more pronounced microscale variations. The used powder's heat map reveals a heterogenous color distribution, signifying a more varied surface topography as opposed to the uniformity observed in the virgin powder's heat map. The surface topology of binder jetted green parts with virgin and used powders revealed a correlation between roughness parameters and relative density. The smoother surface of virgin powder parts aligns with a higher relative density of ~55%, reflecting a more homogenous layering and reduced porosity with an initial level of ~0.45. This would suggest a denser packing of particles, which is conducive to better mechanical bonding and structural consistency, essential for the integrity and dimensional accuracy of the final part. In contrast, the green parts produced with used powder, which exhibited a rougher surface with higher R_a and R_q values, correspond to a lower relative density of ~48% and an increased pore level of ~0.52. This suggests that the surface irregularities and larger particle aggregates in used powder may disrupt layer adhesion and uniform particle distribution. The quantitative surface roughness analysis implied that the lower packing density of the used powder resulted in higher interaction depth and powder displacement on the surface of each layer, in agreement with in-situ observation by Parab et al. [18].

3.3. Microstructure analysis

The microstructural integrity of binder jetted samples, visible through optical micrographs and quantitatively analyzed via distribution of pore sizes and relative densities, is influenced by the feedstock type and the sintering temperatures applied, as depicted in Figure 5. At 1220 °C for 8 h, both used and virgin powder sintered samples demonstrated noticeable porosity. This was characterized by a high density of pores distributed throughout the matrix, with those in the used powder being more numerous and slightly larger, suggesting a wider span of pore sizes. Corresponding to these distributions, the relative densities of the samples are measured to be ~84.9% for used powder and ~89.0% for virgin powder, showing the higher pore associated with the former. With an increase in the sintering temperature to 1340 °C for 8 h, the optical micrographs revealed a decrease in pore number, yet maintaining a higher pore density in the used powder samples. This resulted in a significant enhancement in final part density, with relative densities reaching 87.3% for used powder and a notably higher 96.9% for virgin powder. Such densities align with the observed sharper peaks for virgin powder in the probability density functions, pointing to a homogeneity in smaller pore sizes, while the extended distribution tail for the used powder indicates the inclusion of larger pores.

At the higher sintering temperature of 1370 °C for 8 h, the micrographs showed a continued densification process. The used powder samples maintained a higher pore density compared to the near-full density of virgin powder samples, which was reflected in their relative densities of 94. 7% and 99.2%, respectively. In the sintered specimen printed with virgin powder, a small amount of δ-ferrite phase can be seen within the microstructure. The micrographs correlate with the pore size distributions, where the used powder predominantly displayed retention of smaller pores, and the virgin powder exhibited a notably uniform distribution of pore sizes, primarily at the lower end of the spectrum. The trend continues at the peak temperature of 1400 °C for 8 h, as evidenced by the micrographs

that show an almost fully dense structure for both used and virgin powder binder jetted samples, with minimal and infrequent pores and δ-ferrite phase [35,59,60]. This was further confirmed by relative densities which were measured at ~99.9% for powders. Despite this high density, the used powder samples showed to some extent irregular distribution of pore sizes, suggesting a mix of different pore sizes. In contrast, virgin powder maintains a consistent distribution of predominantly smaller pores.

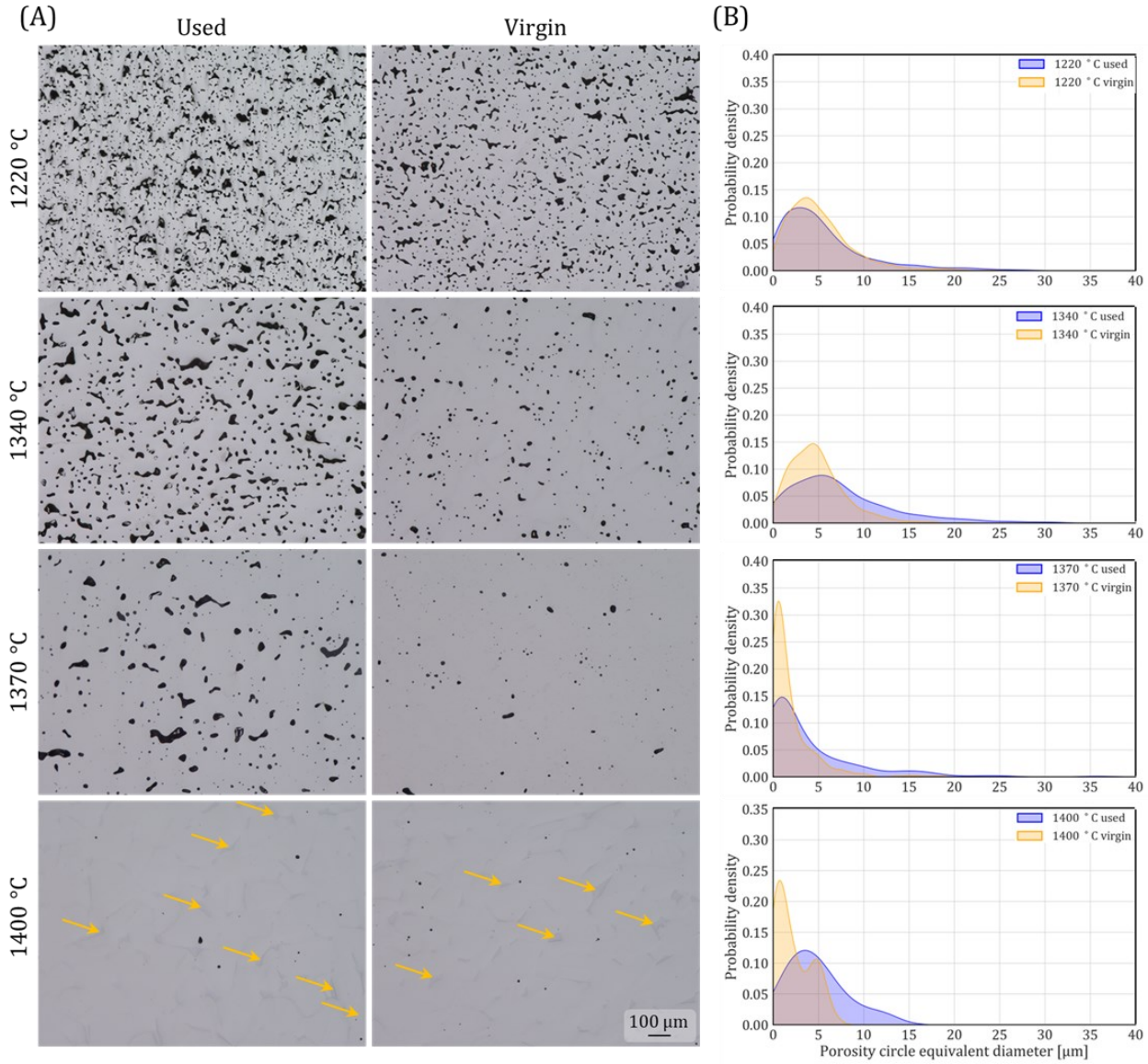

Figure 5. (A) Optical micrographs and (B) probability density function (PDF) plots depicting the pore characteristics of samples fabricated by binder jetting with used and virgin feedstocks, sintered at temperatures ranging from 1220 °C to 1400 °C, showing the interplay between sintering parameters and the resultant pore structure. Arrows show areas in which delt-ferrite appear at the grain boundaries.

The EBSD micrographs in Figure 6 illustrate the evolution of pore elimination and grain growth after sintering of the binder jetted 316L SS across various sintering temperatures with dwell time of 8 h. At 1220 °C, the used powder samples showed a refined microstructure with small, uniformly distributed grains indicative of minimal grain growth and densification.

The virgin powder samples, while still refined, showed slightly larger grains, associated with higher green density and lower pore fraction in the green part. The necking process occurred more rapidly in the binder jetted parts using the virgin powder, initiating grain coarsening at temperatures as low as 1220 °C. Pore counts were higher with more varied pore sizes in the samples printed from the used powder, with notable amounts available at grain boundaries, compared to the more homogenous distribution and reduced pore fraction in the manufactured parts from the virgin powder. Progressing to 1340 °C, both sample types demonstrated grain growth, yet the used powder samples retained higher pore fraction with irregular shapes, contrasting with the virgin samples' trend towards densification and more regular pore morphology. At 1370 °C, the grain growth in manufactured samples from the used powder were diverse, indicating a non-uniform grain structure. Pore continued to diminish, becoming more regular in shape, and primarily located at grain boundaries, suggesting improved densification yet not achieving the density of fabricated samples with virgin powder. Conversely, the virgin powder samples presented a more uniform grain structure with minimal pore. Phase analysis revealed the dominance of the austenitic phase in both powder conditions with no signs of δ-ferrite phase at the grain boundaries. At the peak temperature of 1400 °C, both used and virgin powder samples achieved near-full density (relative bulk density of 99.9%). The phase map showed the presence of δ-ferrite at grain boundaries in both powder conditions, with a quantified area fraction of <2%.

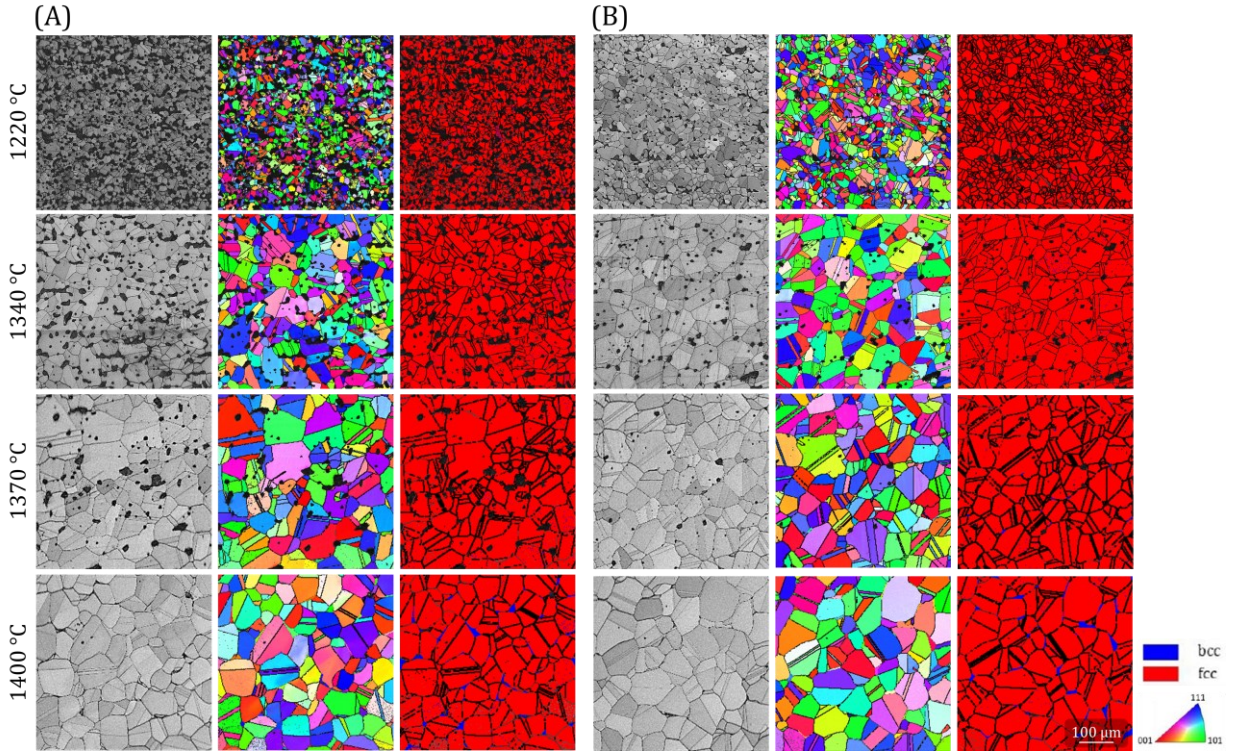

Figure 6. EBSD data sets of the binder jetted 316L SS manufactured with (A) used and (B) virgin feedstock, sintered at 1220 °C-1400 °C for 8 h. Each group of micrographs displays (left) band contrast, (middle) inverse pole figure Y (IPFY), and (right) phase map on Z-direction sections.

Figure 7(A) represents the results of the grain size distribution analysis obtained from EBSD data for the parts binder jetted with virgin and used powders. At 1220 °C, used powders showed a mean grain size of 19.1 µm, closely aligning with the virgin powders which had a

mean of 20.2 μm. The similarity in these values suggested a consistent grain size in the used powders, as highlighted by a narrower standard deviation of 8.8 μm, compared to 10.9 μm for the virgin samples. Both distributions were right-skewed, with the used powders having slightly more pronounced peaks, indicated by skewness values of 1.32 for used and 1.26 for virgin powders, and kurtosis values of 2.25 and 2.03, respectively. The right-skewness suggested a larger number of smaller grains, while the kurtosis values indicated the presence of heavier tails in the distribution. Moving to 1340 °C, a more pronounced difference in grain size distribution was observed. The used powders exhibited mean grain sizes of 38.0 μm, while the virgin powders had a mean grain size of 47.4 μm. Specifically, the distribution for the virgin powder hinted at bimodality, suggesting the presence of two distinct populations of grain sizes, which could indicate varying stages of densification or grain growth. The wider standard deviation in the virgin powders (26.4 μm) compared to the used powders (21.7 μm) represented a broader range of grain sizes. The skewness values of 0.90 for used and 0.62 for virgin powders, coupled with kurtosis values of 0.73 and -0.62, reinforce the right-skewed nature of the distribution, with virgin powders showing a less peaked, flatter distribution.

At 1370 °C and 1400 °C, the analysis mirrored these trends. The used powders at 1370 °C showed a mean grain size of 55.5 μm, close to the virgin powders with a mean of 57.0 μm. At 1400 °C, the used powders exhibited a mean grain size of 57.0 μm, while virgin powders had a mean grain size of 61.6 μm. The standard deviations at these temperatures indicated a more significant spread in the virgin powders. Skewness and kurtosis values consistently showed a right-skewed distribution, with the used powders exhibiting less pronounced peaks compared to the virgin powders. The percentile values (10^{th}, 50^{th}, 90^{th}) across all temperatures revealed a consistently higher proportion of larger grains in the virgin powders, especially evident in the 90^{th} percentile values. This observation is crucial as it indicated a higher likelihood of larger grains in virgin powders, which might influence the material properties and the performance of binder jetted 316L SS parts.

Grain size evolution data is being used in determining sintering stress and viscosity in analytical modeling. To analyze this, the study utilized data from our previous study [57] where isothermal sintering was conducted at 1220, 1340, 1370, and 1400 °C, with eight different dwell times ranging from 0 to 8 h. The mean grain size obtained from EBSD data revealed the trends. The initial grain size was set as the mean powder size, following the recommendation by Jiang and Ning [32]. At 1220 °C, grain growth is minimal, indicative of slower kinetic processes due to the lower thermal energy. As the temperature increases to 1340 °C and 1370 °C, there is a notable increase in grain size, suggesting enhanced atomic diffusion and boundary migration, a clear shift to final stage of sintering. The most pronounced grain growth is observed at 1400 °C. These increments in grain size at higher temperatures are consistent with anticipated sintering behavior, where increased temperatures accelerate diffusion processes, leading to more significant grain growth. This pattern highlighted the material's thermal response, transitioning from restrained to active sintering with the increase in temperature [32–34,57].

In addition, the EBSD data sets revealed trends in grain boundary twinning (high angle grain boundaries, >5°) across different sintering temperatures for both binder jetted parts with used and virgin 316L SS powders. This phenomenon, indicative of certain modes of grain boundary movement and deformation. At 1220 °C, the percentage of twin boundaries in used powder was recorded at ~37%, while the virgin powder exhibited a slightly higher twinning fraction at ~44%. This difference suggests that the microstructural evolution in the

virgin powders might be more conducive to twinning, possibly due to their initial microstructural state or differences in the grain boundary configurations affected by the initial green density. At 1340 °C, the used powders showed a modest increase in twinning to ~41%, whereas the virgin powders demonstrated a slight increase to ~45%. The closer twinning percentages at this temperature indicated a convergence in the microstructural characteristics of the used and virgin powders, potentially due to the temperature-induced homogenization of the grain boundary structures. At 1370 °C, the trend in twinning showed a slight divergence again, with the used powders displaying ~41% and the virgin powders showing a minor decrease to ~44%. This divergence could reflect the differences in the thermally activated mechanisms governing grain boundary movement and twinning in the two powder types. Reaching the peak sintering temperature of 1400 °C, both used and virgin powders exhibited a decrease in twinning, recording ~36% and ~39%, respectively. This trend at the highest temperature suggests that intensified grain growth may restrict new twin formation and alter existing grain boundaries.

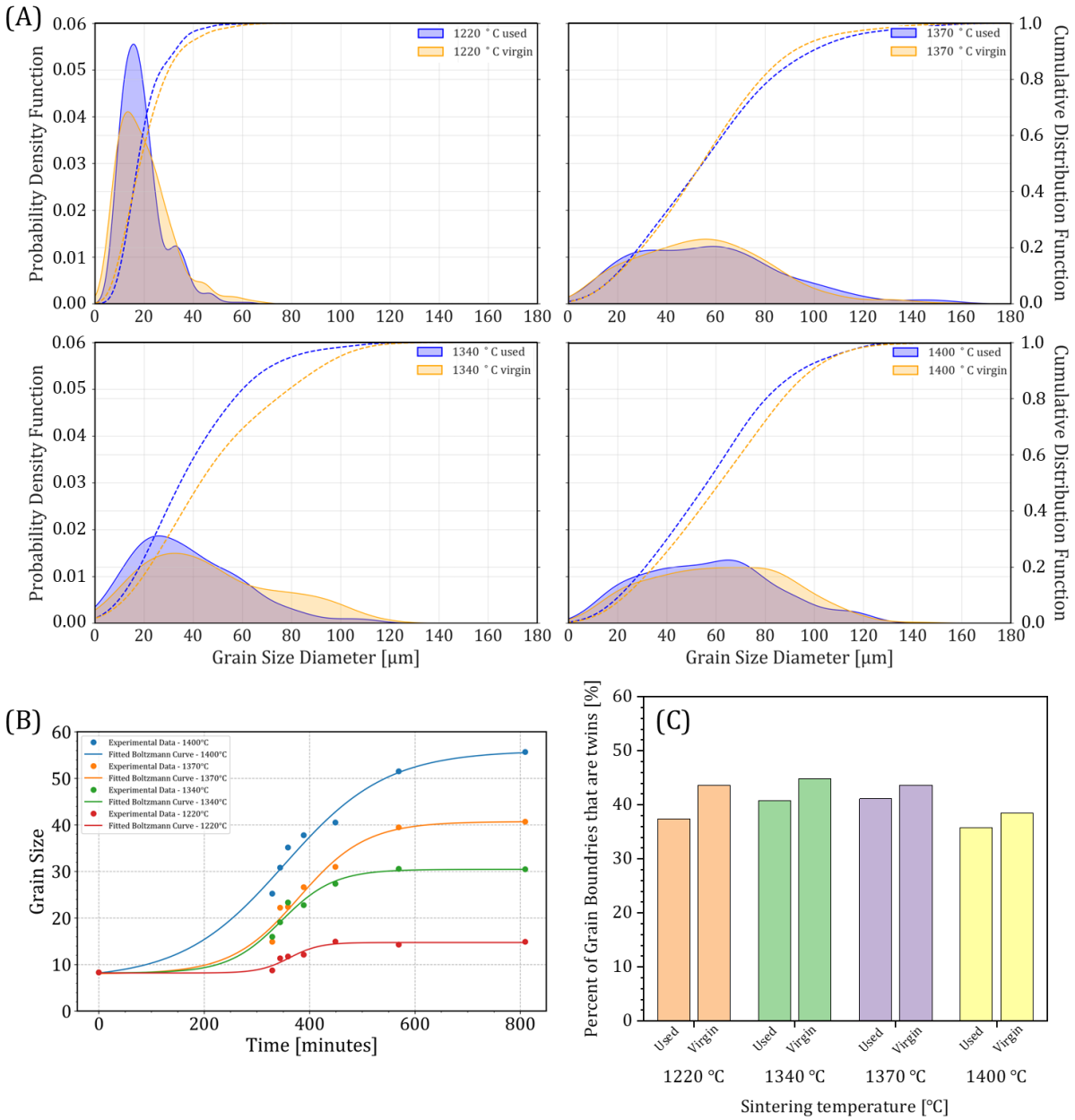

Figure 7. Analysis of grain size in binder jetted samples: (A) PDF and CDF graphs, (B) evolution of grain size, and (C) proportion of grain boundaries with twinning; using both used and virgin powders and sintered at temperatures from 1220 °C to 1400 °C for 8 h.

3.4. Analytical modeling

An essential step involves post-processing the experimental raw data to model the sintering behavior. The relative green density of the binder-jetted specimens was 57±0.5% for the virgin powder and 48.0±1.0% for the used powder. Both values were lower than the powder tap density of 62.0% for the virgin powder and 59.7% for the used powder. The plots of strain, also known as shrinkage, against time for each sintering condition are shown in Figure 8, indicating the evolution of strain in the X, Y, and Z directions during the sintering of binder jetted 316L SS parts. Also, the measured values by caliper were compared with the processed images and results were summarized in Table 2. Since two samples were sintered

for each condition, two values of X (named X1 and X2) are generated from in-situ imaging of XZ and XY planes, respectively.

Different stages of the sintering process can be observed from the plots in Figure 8: (1) *Initial expansion* where the part undergoes expansion is seen during the temperature increase up to 922 °C, particularly in the early section of the plot, (2) *Onset of shrinkage* where the strain values start to decrease and enter negative values, indicating the material is shrinking. It is seen when temperature increases from 922 °C and reaches the applied isothermal sintering temperature, the rate of shrinkage is maximum. (3) *Reduced rate of strain changes* during the isothermal sintering condition, which tends to slow down. (4) *A slight changes in dimensions during cooling phase* suggesting shrinkage proceeds upon cooling from the applied isothermal sintering temperature to the room temperature.

The initial expansion stage of the sintering process is characterized by an appreciable increase in strain across all axes, signifying material expansion. This phase is prominently observed in the early sections of the plots, where the average maximum expansions reach 1.4% in the X1 direction, 1.2% in the X2 direction, 0.7% in the Y direction, and 0.7% in the Z direction. These expansions occurred at an average associated temperature of ~922 °C, indicative of the material's thermal response during the initial heating phase. The observed expansion was also reported by Rios et al. [28] using the dilatometry experiment on binder jetted 316L SS. With the onset of shrinkage, the second stage started as material expansion ended. At the end point of this stage, for instanse at 1220 °C, the shrinkage in the used powder averaged at 5.1±0.4%, while the virgin material showed an average shrinkage of 5.6±0.7%. As the sintering temperature increased to a higher isothermal sintering temperatures including 1340 °C, 1370 °C, and 1400 °C, the average shrinkage values were 9.5±0.7%, 10.7±0.7%, and 14.0±0.5% for the used powder, and 8.3±1.0%, 10.2±1.4%, and 12.0±1.0% for the virgin powder, respectively. This data revealed a trend of increasing average shrinkage with temperature, with the used powder showing a notably higher average shrinkage at 1400 °C. Concurrent with the observed shrinkage, the second stage also displayed an increasing trend in average strain rate with rising sintering temperatures, moving from ~4.85×10^{-4} min^{-1} at 1220 °C to ~8.90×10^{-4} min^{-1} at 1400 °C.

The third stage, occurring during the isothermal sintering phase, was distinguished by a lower strain rate compared to the second stage, with shrinkage changes shifting towards a more plateau-like condition, especially at elevated sintering temperatures (e.g., ≥ 1370 °C). Notably, in the initial 30 min of the isothermal phase at 1370 °C and 1400 °C, a transitional stage was observed with an excessive strain rate as the temperature reached its maximum, revolving towards plateau behavior, particularly in the Z axis, where maximum shrinkage was detected. Such a high strain rate was also recorded in a study by Jiang and Ning in [32] as the sintering happened at temperature of ~1380 °C, and also similar gradual reduction in strain was observed in stage 3 as progressing in holding period. The anisotropy in shrinkage was more pronounced in the virgin powder, with the Y axis generally lagging behind the X and Z axes in terms of maximum shrinkage.

In the final stage, the strain rate slightly increased compared to the end point of the third stage, with a decrease in anisotropy in shrinkage, particularly between the X and Z axes. For 1220 °C (used powder), the shrinkage (seen at the end of the in-situ imaging) was relatively uniform across all axes, 15.6%, 15.4%, and 15.5% in X, Y, and Z directions, respectively. In contrast, for the 1220 °C virgin powder, the shrinkage values were 14.4%,

13.7%, and 15.0% in the X, Y, and Z directions. The used powder showed slightly higher shrinkage with less variability compared to the virgin powder. At higher temperatures, the shrinkage trends varied more distinctly. For the 1340 °C used powder, the shrinkage was 18.2%, 16.7%, and 19.9% in the X, Y, and Z directions, respectively, while the virgin powder showed 13.8%, 12.5%, and 15.4% in the respective directions. At 1370 °C, the used powder exhibited shrinkages of 18.9%, 18.7%, and 20.9%, compared to 16.3%, 15.5%, and 18.1% for the virgin powder, in the X, Y, and Z directions, respectively. The most significant differences were observed at 1400 °C, where the used powder experienced shrinkages of 21.5%, 21.2%, and 23.2%, in contrast to 18.9%, 18.1%, and 20.3% in the virgin powder, X, Y, and Z directions, respectively. Overall, at these three temperatures, the used powder consistently exhibited higher shrinkage across all axes than the virgin powder, with the most significant difference observed in the Z direction, which implies anisotropy in densification of binder jetted materials. All these values were based on the image processing and strain in three dimensions. Results were summarized in Table 2 and compared with actual measurement on samples using caliper. A higher strain or shrinkage in measurements using caliper compared to image processing was associated with the fact that image processing was conducted upon cooling up to ~650 °C. Below this temperature, imaging was stopped due to decreased brightness, and it was not possible to capture images. Thus, the sample continued shrinking for an additional ~1% to room temperature.

Relevant to these observations is the study of sintering anisotropy through dilatometry analysis, which highlighted that the sintering shrinkage and strain rate are greater in the building direction (Z-axis) of the 3D printed parts compared to other directions [32,61]. This behavior signifies the trends observed in the current study, especially in the pronounced shrinkage along the Z-axis, resulting from higher porosity in interlayer space in the powder bed systems associated with the interactions between powder and binder leading to the displacement of powder up to a certain depth in each discrete layer [18] as well as gravitational force induced at Z-axis [32]. Researchers were reported similar anisotropy in sharinkage for different materials such as nickel alloys [29,36], 316L SS [35,62], 17-4 PH SS [31] and copper [63]. In any cases of these materials, microstructure analysis of the densified samples sintered at low temperature showed large areas of pores between the printed layers, which were related to the in-process layer defect generation leading to higher shrinkage in Z-direction. To minimize this issue, higher powder packing density and pre-wetting the surface could minimize powder agglomeration, ejection and interaction depth [19].

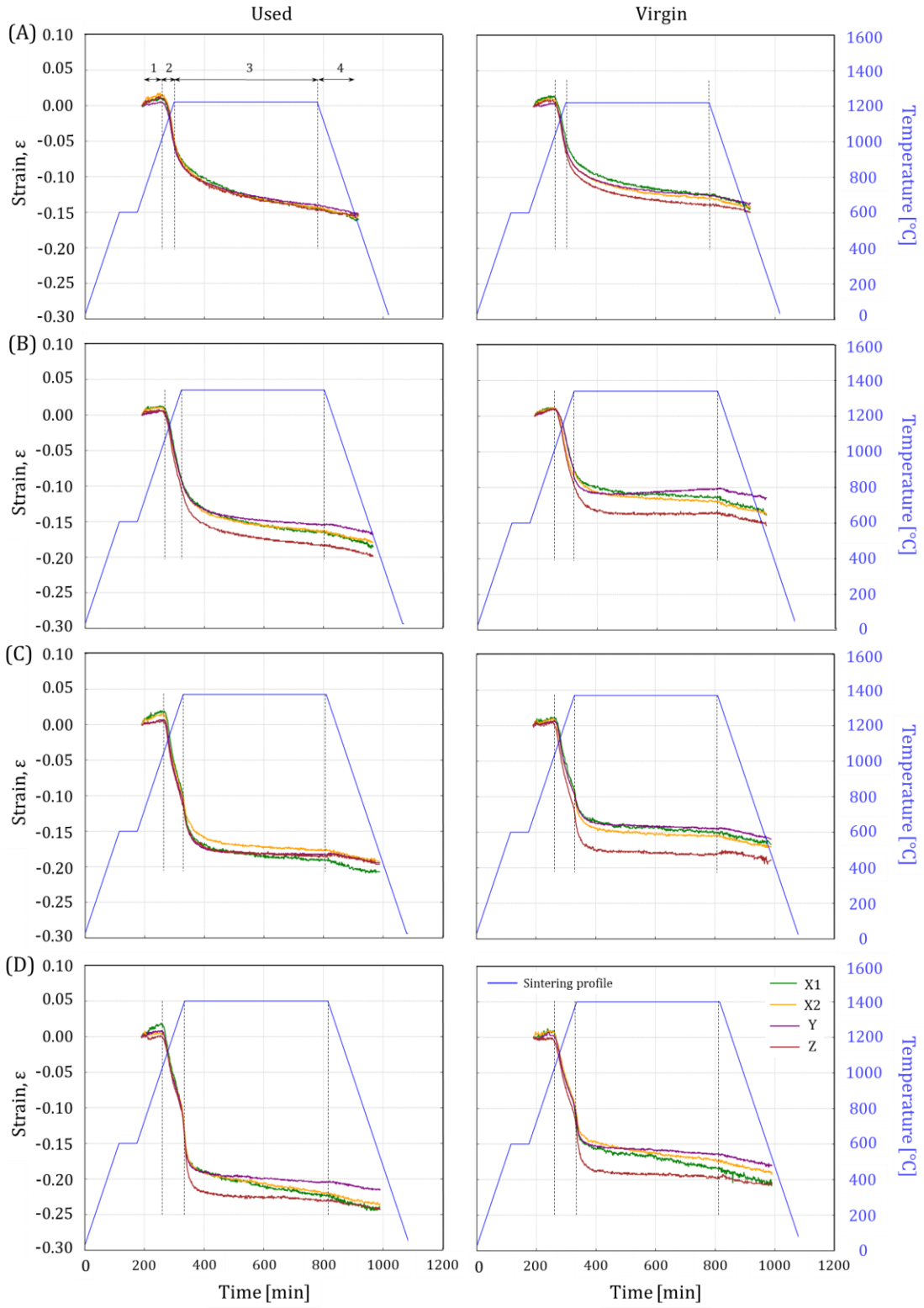

Figure 8. Results of the strain evolution from the in-situ imaging of sintering process of the binder jetted 316L SS using virgin and used powder. Sintering was conducted at (A) 1220 °C, (B) 1340 °C, (C) 1370 °C, (D) 1400 °C. An exemplary labeled regions in "A and used powder" denote (1) initial expansion, (2) Onset of shrinkage, (3) Reduced rate of strain change, and (4) Changes during cooling phase.

Table 2. Strain and relative density results from measurements after sintering experiments.

Sintering condition	Powder	ε_x [%]		ε_y [%]		ε_z [%]		Sintered density [%]
		Caliper	Image processing	Caliper	Image processing	Caliper	Image processing	
1220 °C-8 h	Used	-15.7	-15.6	-15.8	-15.4	-16.8	-15.5	84.9
	Virgin	-14.1	-14.4	-14.4	-13.7	-15.5	-15.0	89.0
1340 °C-8 h	Used	-18.4	-18.2	-17.9	-16.7	-19.6	-19.9	87.3
	Virgin	-15.0	-13.8	-14.3	-12.5	-16.8	-15.4	96.9
1370 °C-8 h	Used	-19.9	-18.9	-19.5	-18.7	-22.4	-20.9	94.7
	Virgin	-16.8	-16.3	-16.5	-15.5	-19.8	-18.1	98.5
1400 °C-8 h	Used	-22.5	-21.5	-22.1	-21.2	-24.3	-23.2	99.9
	Virgin	-19.1	-18.9	-18.8	-18.1	-21.8	-20.3	99.9

Figure 9(A-D) illustrates the evolution of pore fraction upon densification at different temperatures. The initial pore fraction, essential for analytical modeling under the mass conservation law, was assessed based on the pore level of the brown parts (which was after binder burnout step). The final porosity was determined from the solid volume fraction in optical micrographs shown in Figure 5(A). Four distinct stages of evolution of pore fraction were identified during densification, with minor variations between the two orientations (X1YZ and X2YZ) for both powder types.

In stage I, the pore fraction of the green part remained unchanged up to the binder burnout ot debinding stage. After this period, the brown part began to gradually expand, reaching its maximum value at ~922 °C. This maximum pore fraction was ~53% for parts made with used powder and ~47% for those with virgin powder, an increase from the pore fraction measured in the brown part (~52% and 45%, respectively). This would be associated with binder removal, leaving voids behind in the preform structure. Stage II was associated with significant reduction in porosity, occurring as the temperature rose from ~922 °C to the initial peak of the maximum sintering temperature. This remarkable reduction in pores in this stage was also reported by [32]. Stage III was marked by a slower rate of pore reduction compared to Stage II. At 1220 °C and 1340 °C, the rate of pore fraction reduction gradually decreased during the hold time, although the overall trend was steeper compared to 1370 °C and 1400 °C. However, at 1370 °C and 1400 °C, the highest rate of pore reduction occurred within the first hour of sintering at the maximum temperature, before significantly leveling off until the end of the dwell period. It was propounded that the enhanced densification rate could be associated with the formation of δ-ferrite with BCC crystal structure which has higher diffusion coefficient compared to asutenite with FCC phase. This same behavior has been many times observed previously in [28,42,64–67]. Stage III is mostly governed by grain growth as presence of pores was reduced and grain coarsening rate increased [28,68]. In Stage IV, following the hold period at the maximum sintering temperature, the trend of pore reduction persisted downwards, leading to the lowest level of porosity after cooling. No significant difference in the rate of pore reduction was observed at 1220 °C and 1340 °C; however, at 1370 °C and 1400 °C, the rate of decrease was more pronounced compared to Stage III, which was related to the reduction of diffusion pathways caused by grain coarsening thus made the sintering shrinkage rate slow down greatly [32,65]. The lowest porosity levels achieved after sintering were ~22% and ~15% at 1220 °C, ~17% and ~11% at 1340 °C, ~10% and ~7% 1370 °C, and ~3% and ~1% at 1400 °C for parts manufactured using used and virgin feedstock, respectively.

To monitor the evolution of the porosity difference between parts made with used and virgin powder over time, Figure 9(E) was plotted. From the binder burn-out stage to the initial peak of maximum temperature, an increasing trend in the porosity difference between the used and virgin parts was observed, reaching its maximum around the initial peak of maximum temperature. This maximum difference in pore fraction was ~9% across all sintering temperatures. At 1220 °C, a moderate slowdown in this discrepancy was noted as sintering advanced during the dwell period; however, at 1340 °C and beyond, a rapid reduction in this difference occurred, reaching its minimum and stabilized thereafter. As the sintering temperature increased, the discrepancy decreased.

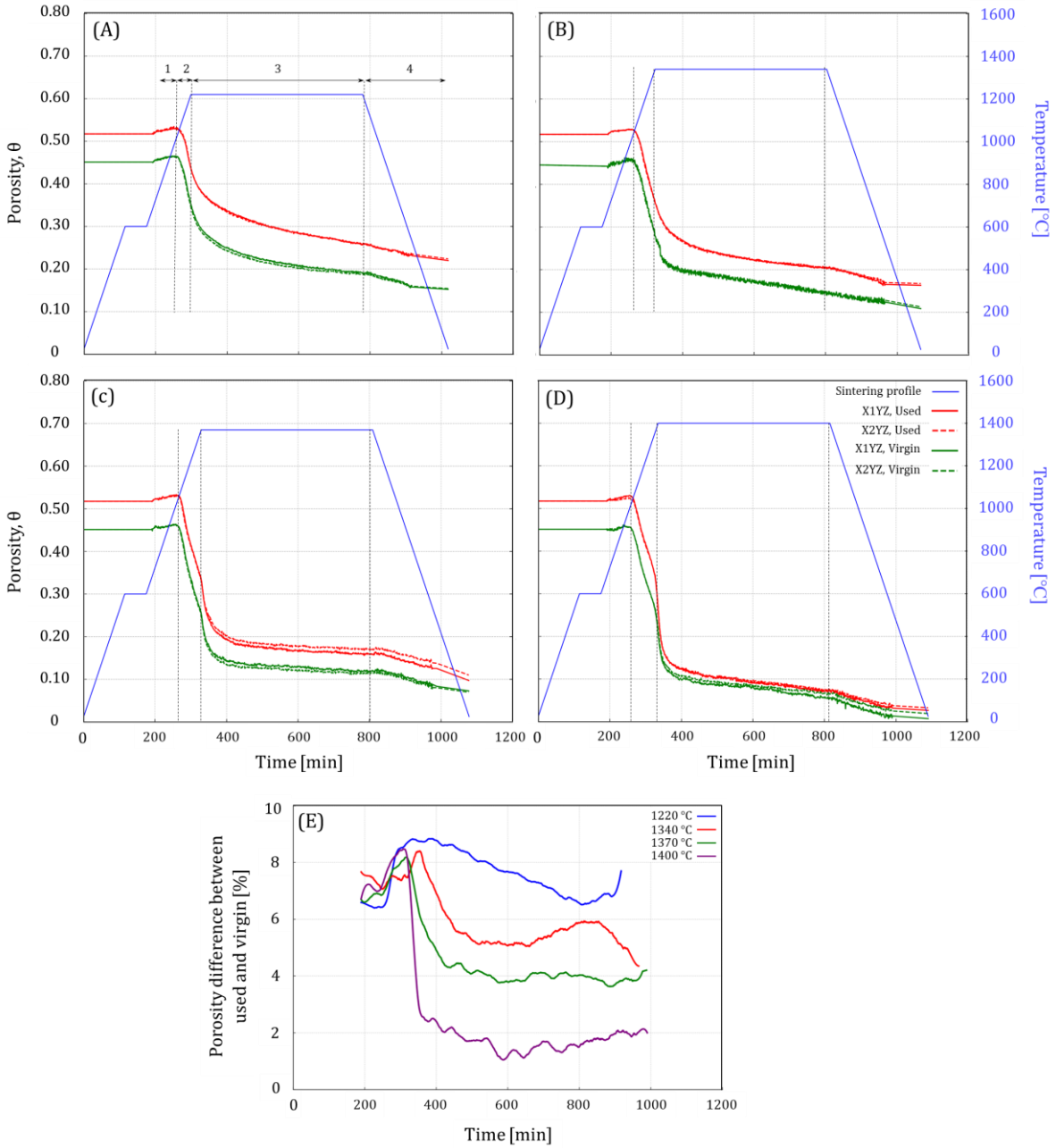

Figure 9. Evolution of porosity in binder jetted 316L SS manufactured with the used and virgin powder over sintering temperatures of (A) 1220 °C, (B) 1340 °C, (C) 1370 °C, and (D) 1400 °C for 8 h, and (E) the comparative evolution of porosity differences between parts made with used and virgin powder.

Solving for anisotropic viscosity (η_x, η_y, and η_z) reveals the viscous behavior of the cubic sample, providing the inputs for the numerical modeling such as finite element simulation [32]. As depicted in Figure 10, the viscosities across the X, Y, and Z directions, corresponding to sintering temperatures ranging from 1220 °C to 1400 °C, reveal significant insights for binder jetted 316L SS using both used and virgin feedstock. Regression analysis (with R^2>95%) indicates a consistent decrease in viscosity with increasing sintering temperatures across all conditions, representing a reduction in the material's resistance to flow under applied sintering stress as the sintering temperature is elevated. At lower sintering temperatures, the disparity in viscosity for components fabricated with used versus virgin powder becomes more pronounced. This trend aligns with the observed variations in viscosity among different directions, where discrepancies between η_x, η_y, and η_z intensify as the sintering temperature decreases. Notably, at elevated sintering temperatures (1370 °C and 1400 °C), where densification approaches it final stage and pore closure is predominant, the viscosity differences in parts produced by used and virgin powders minimized, indicating a convergence towards uniform material behavior. It is noteworthy that lower η values would typically lead to larger shape distortions [28].

Above 1370 °C, the slop of the fitted curves changed in Figure 10, indicative of phase transformation, thus, lower viscosity at the maximum applied sintering temperature of 1400 °C. Formation temperature and fraction of δ-ferrite as well as the presence of a liquid phase significantly influence material diffusivity, both of which are affected by the carbon and oxygen contents, influenced by binder saturation, binder burnout steps, and the residual C/O residue on the powder particle surfaces prior to densification at maximum applied temperatures [35,57,65,69]. The EBSD phase maps in Figure 6 showed no evidence of δ-ferrite up to the applied sintering temperature of 1370 °C, while at the maximum applied temperature of 1400 °C, a small fraction of δ-ferrite was observed at the grain boundaries. Typically, the formation of δ-ferrite at the grains leads to the creation of new grain boundaries, thereby enhancing the densification process. Additionally, a small fraction of the liquid phase facilitates pore filling and the achievement of full density. Rios et al. [70] noted that the formation of δ-ferrite reduced viscosity, enhancing materials diffusion and densification, thus leading to changes in material viscosity at a higher rate.

This behavioral trend is indicative of the complex interplay between sintering temperature and the feedstock's condition and resultant green density of the binder jetted samples on the viscous flow properties. The observed reduction in viscosity with increasing sintering temperature can also be attributed to enhanced particle coalescence and pore reduction, facilitating smoother flow under stress. Conversely, the increased viscosity discrepancies at lower temperatures for used versus virgin powder highlight the impact of feedstock condition on sintering dynamics. Parts manufactured using used powder exhibited altered particle size distribution and powder flowability, attributable to their recycling history. Furthermore, the distinct viscosity values across different axes (η_x, η_y, and η_z) at lower temperatures emphasise the anisotropic nature of material flow during the sintering process of binder jetted specimens. This anisotropy, more pronounced at lower sintering temperatures, suggested directional dependencies in particle rearrangement and densification behavior, which are critical considerations for optimizing sintering protocols and predicting final part properties. As shown in previous investigations [18,29,71], the rearrangement of particles during binder-powder interaction alters the packing density of

the powder bed and creates voids in the area where the binder is deposited. This effect is particularly noticeable in the build direction, leading to increased shrinkage in the Z direction. Additionally, observations of the topology in Figure 4 indicated sequential height changes in the X direction, attributed to the ballistic effect during binder deposition. Therefore, the viscosity in three dimensions is in the order of $\eta_y > \eta_x > \eta_z$. The relationship between lower viscosity values and the potential for increased shape distortions, as highlighted in the literature [32–34,69], emphasizes the importance of understanding and controlling viscosity during sintering to mitigate manufacturing defects and achieve desired geometrical accuracies. These insights underscore the crucial role of sintering temperature and feedstock in dictating the viscous flow behavior of binder jetted 316L SS, with significant implications for the optimization of manufacturing processes and the quality of the final parts.

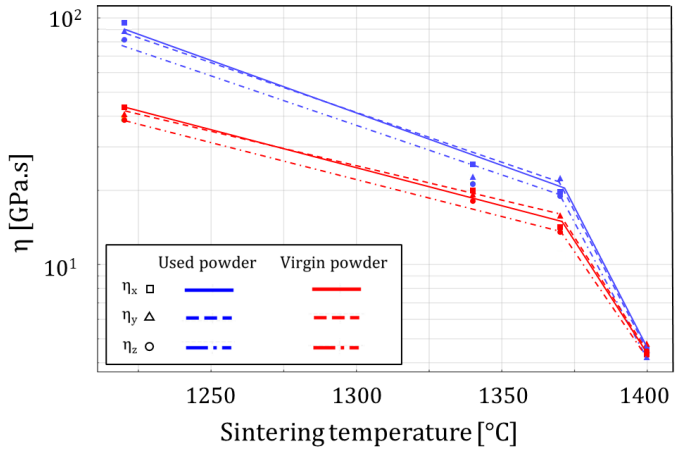

Figure 10. Calculated viscosity of the binder jetted 316L SS utilizing used and virgin feedstock.

Figure 11 presents the relationship between shear and bulk viscosity in relation to porosity for binder jetted parts made from both used and virgin powder, across a range of sintering temperatures, from 1220 °C to 1400 °C. This analysis reveals distinct patterns in viscosity behavior: as porosity diminishes, both shear and bulk viscosity values exhibit an increase. However, the nature of this increase diverges between the two types of viscosity. Bulk viscosity demonstrates an exponential rise as pore fraction decreases, highlighting a pronounced sensitivity to pore changes. In contrast, shear viscosity follows a linear trajectory of increase, suggesting a more uniform adjustment to reductions in porosity. At the lower sintering temperature of 1220 °C, a substantial discrepancy is observed in the viscosity values of parts produced with used versus virgin feedstock, representing the significant impact of feedstock and resultant relative green densities on viscosity behavior. As the sintering temperature increased to 1340 °C and 1370 °C, this disparity obviously diminished, leading to a convergence in viscosity values between parts made from used and virgin powder. This trend suggests that increasing sintering temperatures facilitate microstructure homogenization and therefore uniformity in material properties, regardless of the initial state of the powder and the relative green densities. By the time the sintering temperature reached 1400 °C, differences in viscosity between parts made from used and virgin powder virtually vanish, indicating a near-complete alignment in material behavior. This uniformity

extends across different axes, signifying that at this elevated temperature, the influence of pore fraction and strain rates on viscosity becomes uniformly distributed.

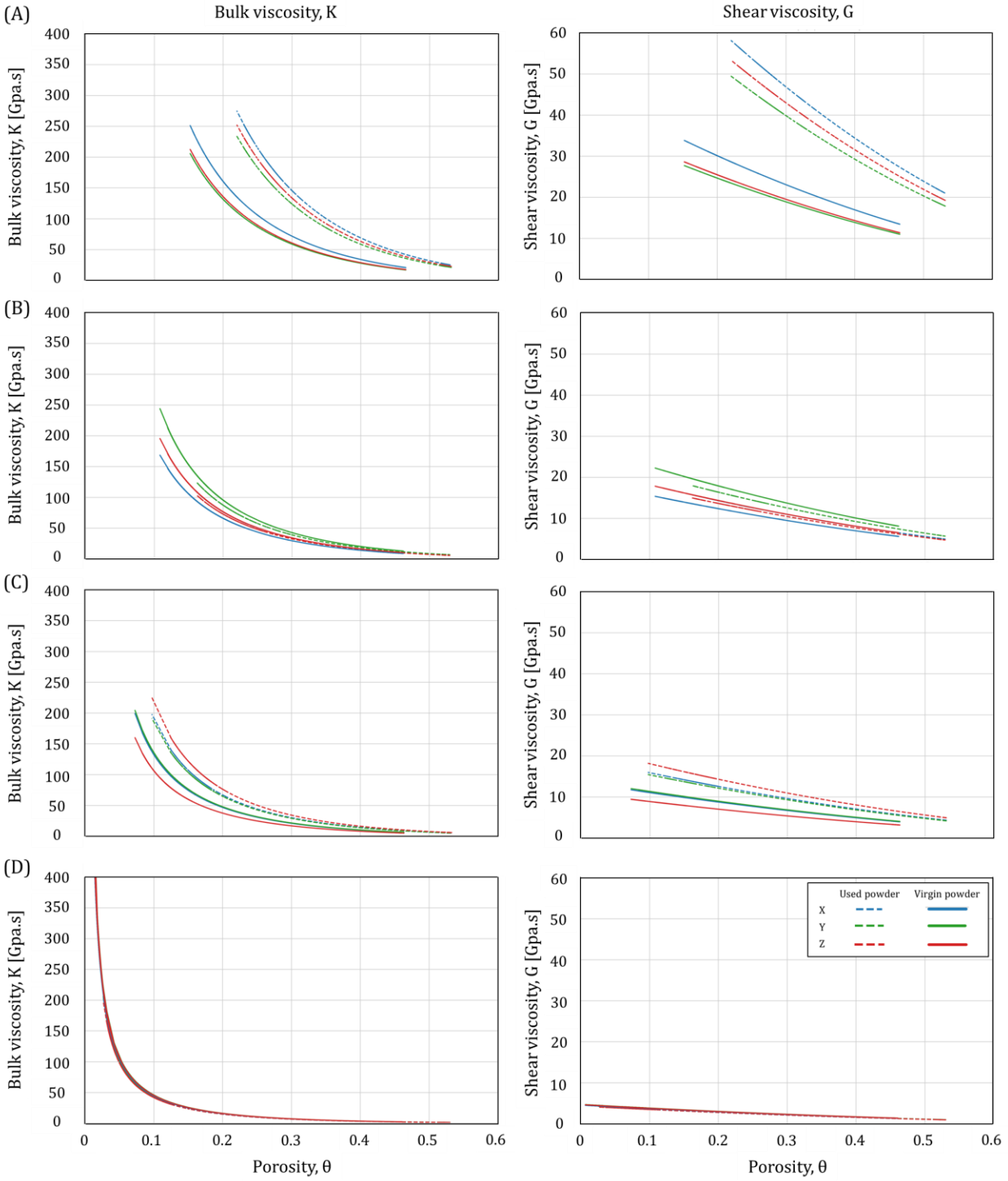

Figure 11. Calculated bulk and shear viscosity during the sintering process of the binder jetted 316L SS utilizing used and virgin feedstock. Sintering was conducted at (A) 1220 °C, (B) 1340 °C, (C) 1370 °C, (D) 1400 °C.

4. Conclusion

The study comprehensively examined the intermediate and final stages of sintering in binder jetted parts fabricated using both virgin and used powders, employing a combination of experimental methods and continuum theory of sintering. The following concluding remarks were made:

- Virgin powder showed a particle size distribution (PSD) of 3.3-18.0 μm and an avalanche angle of 47.4°, with C, O, and N concentrations of 0.025, 0.129, and 0.113 wt.%, respectively. In comparison, the used powder exhibited a PSD of 5.2-19.6 μm, an avalanche angle of 43.4°, with C, O, and N concentrations of 0.029, 0.141, and 0.121 wt.%, respectively.
- Changes in powder characteristics influenced the powder packing density. The green part density of binder jetted components made from virgin powder was 55%, which decreased to 48% for those made from used powder. Surface topology observations indicated a smoother surface finish using virgin powder (R_a = 2.6 μm) compared to used powder (R_a = 7.1 μm).
- Microstructure and pore analysis showed that densification occurred more rapidly in parts binder jetted with virgin powder at temperatures ≤1370 °C. However, a maximum relative density of 99.9% was achieved in any specimen sintered at 1400 °C, associated with supersolidus liquid phase sintering. Significant grain growth, up to ~60 μm, was particularly noted at higher sintering temperatures of 1400 °C with a holding time of 8 h. Electron backscattered diffraction micrographs indicated up to 5% higher twin boundaries in sintered parts printed from virgin powder.
- Using in-situ monitoring, different stages of the sintering process were identified, including (1) initial expansion up to 920 °C, (2) onset of shrinkage between 920 °C and the isothermal sintering temperature, (3) reduced rate of strain changes during isothermal sintering, and (4) slight shrinkage during the cooling to room temperature. This information, extracted through image processing of in-process monitoring observations, was used as input for analytical modeling of sintering and porosity predictions at any holding time.
- By leveraging in-process imaging and experimental data on grain size, the shear and bulk viscosities of the material were determined as $\eta_y > \eta_x > \eta_z$. The calculated viscosities indicated higher shear and bulk viscosities in sintered parts made from used powders. At a sintering temperature of 1400 °C, differences in viscosity between parts made from used and virgin powder disappeared, indicating homogenous, pore-free parts were achieved.

Acknowledgements

AM would like to acknowledge the startup funding from the Department of Mechanical, Materials and Aerospace Engineering and Armour College of Engineering at Illinois Institute of Technology at Chicago, Illinois. Also, partial support from the National Science Foundation under grant number DMR-2050916 and CMMI-2339857 is appreciated by all authors.

References

[1] H. Miyanaji, M. Orth, J.M. Akbar, L. Yang, Process development for green part printing using binder jetting additive manufacturing, Front. Mech. Eng. 13 (2018) 504–512.

[2] L. Cordova, A. Raza, E. Hryha, Rheological Behavior of Inconel 718 Powder for Electron-Beam Melting, (2022).

[3] S. Mirzababaei, B.K. Paul, S. Pasebani, Metal Powder Recyclability in Binder Jet Additive Manufacturing, Jom. 72 (2020) 3070–3079.

[4] A. Mostafaei, C. Zhao, Y. He, S. Reza Ghiaasiaan, B. Shi, S. Shao, N. Shamsaei, Z. Wu, N. Kouraytem, T. Sun, J. Pauza, J. V. Gordon, B. Webler, N.D. Parab, M. Asherloo, Q. Guo, L. Chen, A.D. Rollett, Defects and anomalies in powder bed fusion metal additive manufacturing, Curr. Opin. Solid State Mater. Sci. 26 (2022) 100974.

[5] Z. Snow, R. Martukanitz, S. Joshi, On the development of powder spreadability metrics and feedstock requirements for powder bed fusion additive manufacturing, Addit. Manuf. 28 (2019) 78–86.

[6] M.Z. Gao, B. Ludwig, T.A. Palmer, Impact of atomization gas on characteristics of austenitic stainless steel powder feedstocks for additive manufacturing, Powder Technol. 383 (2021) 30–42.

[7] M. Khademitab, M. Jamalkhani, K. Bishaj, E. Jenssen, M. Heim, D. Nelson, N.M. O'Dowd, A. Mostafaei, Does Selective Shell Printing Advance Binder Jetting Additive Manufacturing?, Powder Technol. 441 (2024) 119812.

[8] A.T. Sutton, C.S. Kriewall, M.C. Leu, J.W. Newkirk, Powders for Additive Manufacturing Processes: Characterization Techniques and Effects on Part Properties, Solid Free. Fabr. Proc. (2016) 1004–1030.

[9] A.T.T. Sutton, C.S.S. Kriewall, S. Karnati, M.C.C. Leu, J.W.W. Newkirk, Characterization of AISI 304L stainless steel powder recycled in the laser powder-bed fusion process, Addit. Manuf. 32 (2020).

[10] P. Nandwana, W.H. Peter, R.R. Dehoff, L.E. Lowe, M.M. Kirka, F. Medina, S.S. Babu, Recyclability Study on Inconel 718 and Ti-6Al-4V Powders for Use in Electron Beam Melting, Metall. Mater. Trans. B. 47 (2016) 754–762.

[11] G. Jacob, C.U. Brown, A. Donmez, S.S. Watson, M.A. Donmez, S.S. Watson, Effects of powder recycling on stainless steel powder and built material properties in metal powder bed fusion processes, 2017.

[12] M. Dorula, M. Khademitab, M. Jamalkhani, A. Mostafaei, Location dependency of green density and dimension variation in binder jetted parts, Int. J. Adv. Manuf. Technol. 132 (2024) 2853–2861.

[13] M. Li, G. Miao, W. Du, Z. Pei, C. Ma, Difference between powder bed density and green density for a free-flowing powder in binder jetting additive manufacturing, J. Manuf. Process. 84 (2022) 448–456.

[14] G. Miao, W. Du, Z. Pei, C. Ma, A literature review on powder spreading in additive manufacturing, Addit. Manuf. 58 (2022) 103029.

[15] A.M. Elliott, C.L. Cramer, P. Nandwana, M. Chmielus, A. Mostafaei, Binder Jet-Metals, Encycl. Mater. Met. Alloy. 3 (2022) 120–133.

[16] A. Mostafaei, A.M. Elliott, J.E. Barnes, C.L. Cramer, P. Nandwana, M. Chmielus, Binder jet 3D printing - process parameters, materials, properties, modeling, and challenges, Prog. Mater. Sci. 119 (2021) 100707.

[17] M. Mariani, N. Lecis, A. Mostafaei, Binder Jetting-based Metal Printing, in: Solid-State Met. Addit. Manuf. Physics, Process. Mech. Prop. Appl., John Wiley & Sons, 2024: pp. 339–357.

[18] N.D. Parab, J.E. Barnes, C. Zhao, R.W. Cunningham, A.D. Rollett, T. Sun, Real time observation of binder jetting printing process using high-speed X-ray imaging, Sci. Rep. (2019) 28–30.

[19] C.G. Inkley, J. Lawrence, N.B. Crane, Impact of Controlled Prewetting on Part Formation in

Binder Jet Additive Manufacturing, Addit. Manuf. 72 (2023) 103619.
[20] J.J. Frenkel, Viscous flow of crystalline bodies under the action of surface tension, J. Phys. 9 (1945) 385.
[21] W.B. Li, H.Å. Häggblad, Constitutive laws for hot isostatic pressing of powder compact, Powder Metall. 40 (1997) 279–281.
[22] R.K. Bordia, G.W. Scherer, On constrained sintering-I. Constitutive model for a sintering body, Acta Metall. 36 (1988) 2393–2397.
[23] V. V. Skorokhod, E.A. Olevskii, M.B. Shtern, Continuum theory of sintering. I. Phenomenological model. Analysis of the effect of external forces on the kinetics of sintering, Powder Metall. Met. Ceram. 32 (1993) 21–26.
[24] F. Raether, G. Seifert, H. Ziebold, Simulation of Sintering across Scales, Adv. Theory Simulations. 2 (2019) 1900048.
[25] E. Olevsky, A. Molinari, Instability of sintering of porous bodies, Int. J. Plast. 16 (2000) 1–37.
[26] T. Kraft, H. Riedel, Numerical simulation of solid state sintering; model and application, J. Eur. Ceram. Soc. 24 (2004) 345–361.
[27] B.J. Paudel, A.C. To, A. Mostafaei, Principles of Solid-State Sintering, in: Solid-State Met. Addit. Manuf. Physics, Process. Mech. Prop. Appl., John Wiley & Sons, 2024: pp. 297–312.
[28] A. Cabo-Rios, E.A. Olevsky, E. Hryha, M. Persson, R.K. Bordia, Analytical models for initial and intermediate stages of sintering of additively manufactured stainless steel, Acta Mater. 249 (2022) 118822.
[29] C. Zheng, A. Mostafaei, P.R. de Vecchis, I. Nettleship, M. Chmielus, Microstructure evolution for isothermal sintering of binder jet 3D printed alloy 625 above and below the solidus temperature, Addit. Manuf. 47 (2021) 102276.
[30] A. Mostafaei, Powder bed binder jet 3D printing of Alloy 625: Microstructural evolution, densification kinetics and mechanical properties (thesis), University of Pittsburgh, 2018.
[31] D. Huber, L. Vogel, A. Fischer, The effects of sintering temperature and hold time on densification, mechanical properties and microstructural characteristics of binder jet 3D printed 17-4 PH stainless steel, Addit. Manuf. 46 (2021) 102114.
[32] D. Jiang, F. Ning, Anisotropic deformation of 316L stainless steel overhang structures built by material extrusion based additive manufacturing, Addit. Manuf. 50 (2022) 102545.
[33] F. Wang, S. You, D. Jiang, X. Yuan, R. Fu, F. Ning, Microstructure evolution, phase formation, corrosion, and mechanical properties of stainless steel fabricated by extrusion-based sintering-assisted additive manufacturing, Addit. Manuf. 75 (2023) 103746.
[34] S. You, D. Jiang, F. Wang, F. Ning, Anisotropic sintering shrinkage behavior of stainless steel fabricated by extrusion-based metal additive manufacturing, J. Manuf. Process. 101 (2023) 1508–1520.
[35] M. Jamalkhani, M. Asherloo, O. Gurlekce, I.-T. Ho, M. Heim, D. Nelson, A. Mostafaei, Deciphering microstructure-defect-property relationships of vacuum-sintered binder jetted fine 316L austenitic stainless steel powder, Addit. Manuf. 59 (2022) 103133.
[36] A. Mostafaei, P. Rodriguez De Vecchis, I. Nettleship, M. Chmielus, Effect of powder size distribution on densification and microstructural evolution of binder-jet 3D-printed alloy 625, Mater. Des. 162 (2019) 375–383.
[37] K. Myers, A. Paterson, T. Iizuka, A. Klein, The Effect of Print Speed on Surface Roughness and Density Uniformity of Parts Produced Using Binder Jet 3D Printing, Solid Free. Fabr. 2019 Proc. 30th Annu. Int. (2019) 122–133.
[38] T. Rosnitschek, S. Tremmel, A. Seefeldt, B. Alber-Laukant, T. Neumeyer, V. Altstädt, Correlations of geometry and infill degree of extrusion additively manufactured 316l stainless steel components, Materials (Basel). 14 (2021).
[39] S.O. Obadimu, K.I. Kourousis, Shrinkage behaviour of material extrusion steel 316L: influence of primary 3D printing parameters, Rapid Prototyp. J. 28 (2022) 92–101.

[40] I. Ait-Mansour, N. Kretzschmar, S. Chekurov, M. Salmi, J. Rech, Design-dependent shrinkage compensation modeling and mechanical property targeting of metal FFF, Prog. Addit. Manuf. 5 (2020) 51–57.
[41] Y. Abe, T. Kurose, M.V.A. Santos, Y. Kanaya, A. Ishigami, S. Tanaka, H. Ito, Effect of layer directions on internal structures and tensile properties of 17-4ph stainless steel parts fabricated by fused deposition of metals, Materials (Basel). 14 (2021) 1–12.
[42] N. Lecis, M. Mariani, R. Beltrami, L. Emanuelli, R. Casati, M. Vedani, A. Molinari, Effects of process parameters, debinding and sintering on the microstructure of 316L stainless steel produced by binder jetting, Mater. Sci. Eng. A. 828 (2021) 142108.
[43] Y. Wu, D. Blaine, B. Marx, C. Schlaefer, R.M. German, Sintering densification and microstructural evolution of injection molding grade 17-4 PH stainless steel powder, Metall. Mater. Trans. A Phys. Metall. Mater. Sci. 33 (2002) 2185–2194.
[44] J. Wang, H. Su, K. Chen, D. Du, L. Zhang, Z. Shen, Effect of δ-ferrite on the stress corrosion cracking behavior of 321 stainless steel, Corros. Sci. 158 (2019) 108079.
[45] X. Chen, J. Li, X. Cheng, H. Wang, Z. Huang, Effect of heat treatment on microstructure, mechanical and corrosion properties of austenitic stainless steel 316L using arc additive manufacturing, Mater. Sci. Eng. A. 715 (2018) 307–314.
[46] C.T. Kwok, S.L. Fong, F.T. Cheng, H.C. Man, Pitting and galvanic corrosion behavior of laser-welded stainless steels, J. Mater. Process. Technol. 176 (2006) 168–178.
[47] G.R. Mirshekari, E. Tavakoli, M. Atapour, B. Sadeghian, Microstructure and corrosion behavior of multipass gas tungsten arc welded 304L stainless steel, Mater. Des. 55 (2014) 905–911.
[48] X. Feaugas, On the origin of the tensile flow stress in the stainless steel AISI 316L at 300 K: Back stress and effective stress, Acta Mater. 47 (1999) 3617–3632.
[49] A. Lukežič, T. Vojíř, L. Čehovin Zajc, J. Matas, M. Kristan, Discriminative Correlation Filter Tracker with Channel and Spatial Reliability, Int. J. Comput. Vis. 126 (2018) 671–688.
[50] M. Jamalkhani, B. Nathan, M. Heim, D. Nelson, A. Mostafaei, Fatigue behavior of vacuum-sintered binder jetted fine 316L stainless steel powder, Mater. Sci. Eng. A. 873 (2023) 144937.
[51] E.A. Olevsky, Theory of sintering: from discrete to continuum, Mater. Sci. Eng. R Reports. 23 (1998) 41–100.
[52] M. Yakout, M.A. Elbestawi, S.C. Veldhuis, Density and mechanical properties in selective laser melting of Invar 36 and stainless steel 316L, J. Mater. Process. Technol. 266 (2019) 397–420.
[53] J.K. Mackenzie, R. Shuttleworth, A Phenomenological Theory of Sintering, Proc. Phys. Soc. Sect. B. 62 (1949) 833–852.
[54] H. Fukuyama, H. Higashi, H. Yamano, Thermophysical Properties of Molten Stainless Steel Containing 5 mass % B4C, Nucl. Technol. 205 (2019) 1154–1163.
[55] M.W. Reiterer, K.G. Ewsuk, J.G. Argüello, An arrhenius-type viscosity function to model sintering using the Skorohod-Olevsky viscous sintering model within a finite-element code, J. Am. Ceram. Soc. 89 (2006) 1930–1935.
[56] V.V. Skorohod, Rheological Basis of the Theory of Sintering, Nauk Dumka, Kiev. (1972).
[57] M. Jamalkhani, E. Roberts, M. Dorula, A. Mostafaei, Densification kinetics, microstructural evolution and mechanical properties of isothermally sintered binder jetted 316L stainless steel, Submitted. (2024).
[58] A. Mostafaei, C. Hilla, E.L.E. Stevens, P. Nandwana, A.M. Elliott, M. Chmielus, Comparison of characterization methods for differently atomized nickel-based alloy 625 powders, Powder Technol. 333 (2018) 180–192.
[59] P. Kumar, R. Jayaraj, J. Suryawanshi, U.R. Satwik, J. McKinnell, U. Ramamurty, Fatigue strength of additively manufactured 316L austenitic stainless steel, Acta Mater. 199 (2020) 225–239.
[60] S. Mirzababaei, B.K. Paul, S. Pasebani, Microstructure-property relationship in binder jet produced and vacuum sintered 316 L, Addit. Manuf. 53 (2022) 102720.

[61] C. Manière, G. Kerbart, C. Harnois, S. Marinel, Modeling sintering anisotropy in ceramic stereolithography of silica, Acta Mater. 182 (2020) 163–171.
[62] Y. Mao, C. Cai, J. Zhang, Y. Heng, K. Feng, D. Cai, Q. Wei, Effect of sintering temperature on binder jetting additively manufactured stainless steel 316L: densification, microstructure evolution and mechanical properties, J. Mater. Res. Technol. 22 (2023) 2720–2735.
[63] A.Y. Kumar, J. Wang, Y. Bai, S.T. Huxtable, C.B. Williams, Impacts of process-induced porosity on material properties of copper made by binder jetting additive manufacturing, Mater. Des. (2019) 108001.
[64] J. Song, T. Barriere, B. Liu, J.C. Gelin, G. Michel, Experimental and numerical analysis on sintering behaviours of injection moulded components in 316L stainless steel powder, Powder Metall. 53 (2010) 295–304.
[65] A.C. Rios, E. Hryha, E. Olesvsky, P. Harlin, Sintering anisotropy of binder jetted 316L stainless steel: part I – sintering anisotropy, Powder Metall. (2021).
[66] A. Cabo Rios, E. Hryha, E. Olevsky, P. Harlin, Sintering anisotropy of binder jetted 316L stainless steel: part I–sintering anisotropy, Powder Metall. 65 (2022) 273–282.
[67] R. Batmaz, A. Zardoshtian, T.D. Sabiston, R. Tangestani, A. Chakraborty, N. Krutz, S. Pendurti, A. Natarajan, E. Martin, An Investigation into Sinterability Improvements of 316L Binder Jet Printed Parts, Metall. Mater. Trans. A Phys. Metall. Mater. Sci. 53 (2022) 915–926.
[68] M. Zou, W.G. Jiang, Q.H. Qin, Y.C. Liu, M.L. Li, Optimized XGBoost Model with Small Dataset for Predicting Relative Density of Ti-6Al-4V Parts Manufactured by Selective Laser Melting, Materials (Basel). 15 (2022).
[69] A.C. Rios, E. Hryha, E. Olesvsky, P. Harlin, Sintering anisotropy of binder jetted 316L stainless steel: part II – microstructure evolution during sintering, Powder Metall. 65 (2022) 283–295.
[70] C.R. Alberto, E.A. Olevsky, E. Hryha, M. Persson, Modelling of δ-ferrite transformation effect on the sintering behaviour of 316L binder jetted components, WorldPM 2022. (2022).
[71] J.J. Wagner, H. Shu, R. Kilambi, C.F.H. Iii, EXPERIMENTAL INVESTIGATION OF FLUID-PARTICLE INTERACTION IN BINDER JET 3D PRINTING, Solid Free. Fabr. 2019 Proc. 30th Annu. Int. (2019) 134–147.